Cell

Condensed Chromatin Behaves like a Solid on the Mesoscale *In Vitro* and in Living Cells

Graphical Abstract

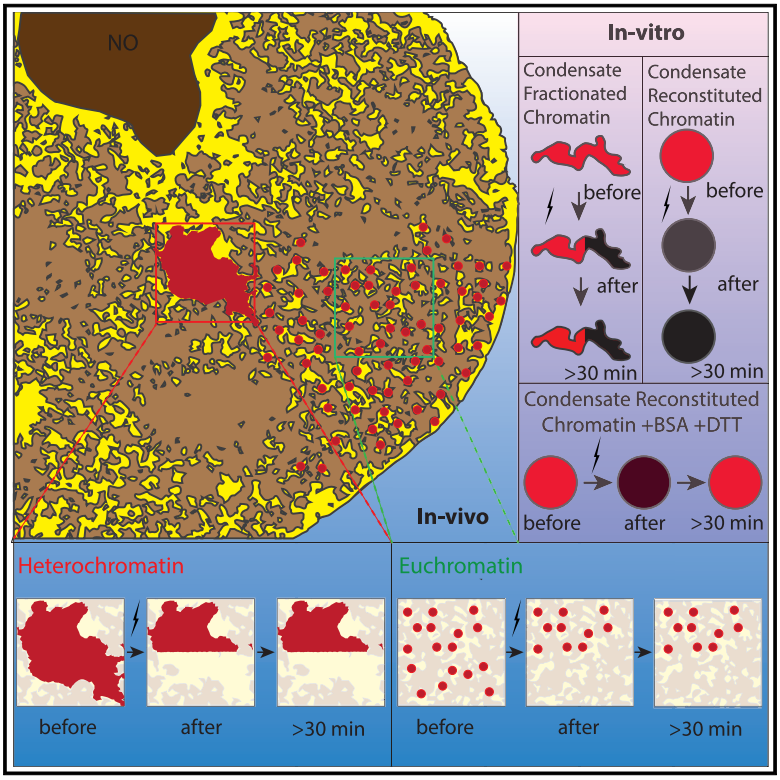

Highlights

- Nucleosome arrays and isolated chromatin are solids under physiological conditions
- Chromatin is solid-like in living cells in high- and low-chromatin-density regions
- Histone acetylation disperses but does not liquify chromatin
- Solid chromatin scaffold supports liquid phase-separated compartments

Authors

Hilmar Strickfaden, Thomas O. Tolsma, Ajit Sharma, D. Alan Underhill, Jeffrey C. Hansen, Michael J. Hendzel

Correspondence

jeffrey.c.hansen@colostate.edu (J.C.H.), mhendzel@ualberta.ca (M.J.H.)

In Brief

Chromatin in live cells functions as a solid material and provides a scaffold for spatial organization of nuclear components that can adopt a liquid-like state.

Strickfaden et al., 2020, Cell *183*, 1772–1784
December 23, 2020
https://doi.org/10.1016/j.cell.2020.11.027

CellPress

CellPress

Cell

Article

Condensed Chromatin Behaves like a Solid on the Mesoscale *In Vitro* and in Living Cells

Hilmar Strickfaden,[3] Thomas O. Tolsma,[4] Ajit Sharma,[3] D. Alan Underhill,[2,3] Jeffrey C. Hansen,[4,5,*] and Michael J. Hendzel[1,3,5,6,*]

[1]Department of Cell Biology, Faculty of Medicine and Dentistry, University of Alberta, Edmonton, AB, Canada
[2]Department of Medical Genetics, Faculty of Medicine and Dentistry, University of Alberta, Edmonton, AB, Canada
[3]Department of Oncology, Faculty of Medicine and Dentistry, University of Alberta, Edmonton, AB, Canada
[4]Department of Biochemistry and Molecular Biology, College of Natural Sciences, Colorado State University, Fort Collins, CO, USA
[5]Senior author
[6]Lead Contact
*Correspondence: jeffrey.c.hansen@colostate.edu (J.C.H.), mhendzel@ualberta.ca (M.J.H.)
https://doi.org/10.1016/j.cell.2020.11.027

SUMMARY

The association of nuclear DNA with histones to form chromatin is essential for temporal and spatial control of eukaryotic genomes. In this study, we examined the physical state of condensed chromatin *in vitro* and *in vivo*. Our *in vitro* studies demonstrate that self-association of nucleosomal arrays under a wide range of solution conditions produces supramolecular condensates in which the chromatin is physically constrained and solid-like. By measuring DNA mobility in living cells, we show that condensed chromatin also exhibits solid-like behavior *in vivo*. Representative heterochromatin proteins, however, display liquid-like behavior and coalesce around the solid chromatin scaffold. Importantly, euchromatin and heterochromatin show solid-like behavior even under conditions that produce limited interactions between chromatin fibers. Our results reveal that condensed chromatin exists in a solid-like state whose properties resist external forces and create an elastic gel and provides a scaffold that supports liquid-liquid phase separation of chromatin binding proteins.

INTRODUCTION

The structural organization of chromatin in the nucleus remains poorly understood (Bian and Belmont, 2012; Eltsov et al., 2008; Fussner et al., 2011; Joti et al., 2012; Maeshima et al., 2010a, 2016b; Ou et al., 2017). Long-standing hierarchical models of chromatin folding have largely been disproven, and new models based on clustering of nucleosomes (Otterstrom et al., 2019; Ricci et al., 2015) and extended 10-nm chromatin fibers (Fussner et al., 2012; Maeshima et al., 2010b, 2016b) into compact chromatin domains (Hansen et al., 2018) have taken their place. In these new models, interphase and mitotic chromosomes are assembled from 10-nm chromatin without subsequent helical coiling. Concomitantly, although the classical 30-nm fiber may be present locally throughout the genome, folded helical fibers are now thought to be absent in bulk from most animal cells and tissues. Although the evidence in favor of models lacking the 30-nm fiber is substantial, the mechanisms by which extended 10-nm fibers are packaged into higher-order heterochromatin and euchromatin domains have not been established. It is widely held that the biophysical properties associated with condensed chromatin are regulatory in nature. Consequently, determining the physical state of condensed chromatin is critical for understanding mechanisms that modulate genome function.

Concomitant with the new models of chromatin organization in the nucleus, *in vitro* studies of chromatin dynamics have also shifted focus. After decades of emphasis on 30-nm fibers (Hansen, 2002; Thoma et al., 1979), recent studies have investigated the process by which chromatin condenses into supramolecular aggregates (Gibson et al., 2019; Maeshima et al., 2016b, Maeshima et al., 2020), to which we refer to as chromatin condensates. Folded 30-nm structures are first observed when cations are titrated into a purified chromatin sample (Finch and Klug, 1976; Thoma et al., 1979). At higher cation concentrations that better approximate those found *in vivo* (Strick et al., 2001), chromatin assembles into condensates. Chromatin condensates have been studied for many years. Historically, chromatin condensates were first referred to as precipitants or insoluble aggregates based on their size and the ease with which they pelleted upon centrifugation. Nevertheless, condensate assembly is freely reversible and requires the core histone tail domains (Gordon et al., 2005; Schwarz et al., 1996), suggesting that chromatin self-interaction is biologically relevant. The structural features of chromatin condensates formed by defined 12-mer nucleosomal arrays in 4–10 mM $MgCl_2$ have been determined recently (Maeshima et al., 2016b). The condensates had a globular morphology and reached 0.5–1.0 μm in diameter, as judged by fluorescence and electron microscopy. Sedimentation velocity

experiments indicated that the condensates sedimented in the 300,000 S range, documenting that these globular structures are stable in solution (Maeshima et al., 2016b). The nucleosomal arrays that made up the condensates were packaged as irregular 10-nm fibers, as is the case with bulk chromatin *in vivo* (Eltsov et al., 2008; Fussner et al., 2012; Ou et al., 2017). However, one feature that was not determined by Maeshima et al. (2016b) was the physical state of packaged nucleosomal arrays in condensates. This question was recently addressed by Gibson et al. (2019), who concluded that condensate formation was driven by liquid-liquid phase separation (LLPS) to produce liquid droplets, leading them to speculate that the material state of chromatin *in vivo* is also liquid.

Indirect evidence of the existence of liquid chromatin *in vitro* and *in vivo* comes from studies of chromatin binding proteins (CBX2, CBX5, MeCP2, SUV39H1, and TRIM28) that can undergo LLPS at micromolar concentrations in near-physiological buffers. The related chromobox proteins HP1apha (CBX5) (Larson et al., 2017) and CBX2 (Tatavosian et al., 2019), which bind to chromatin via trimethylated lysine 9 of histone H3 and trimethylated lysine 27 of histone H3, respectively, undergo LLPS at low micromolar concentrations in buffers containing 100–200 mM monovalent ions. When condensates were formed in the presence of nucleosomes or nucleosomal arrays, they co-partition in the condensate (Larson et al., 2017; Plys et al., 2019; Wang et al., 2019). MeCP2 is a chromatin and methyl DNA binding protein associated with pericentric heterochromatin in vertebrates. MeCP2 forms liquid condensates *in vitro* only in the presence of DNA or nucleosomes (Wang et al., 2020). Based on these *in vitro* experiments, the morphology of the related constitutive and facultative heterochromatin compartments in cells (Larson et al., 2017; Plys et al., 2019; Strom et al., 2017; Tatavosian et al., 2019), and evidence that these proteins move in and out of heterochromatin in living cells (Strom et al., 2017), it has been proposed that the constitutive and facultative heterochromatin structures found in cells are formed and maintained by liquid-liquid unmixing and phase separation of the associated chromatin binding proteins. In this model, chromatin is a passive player, and LLPS is driven by the intrinsic properties of the proteins bound to chromatin.

Despite the attractiveness of liquid condensate formation as a mechanism to explain chromatin packaging and condensation, the contribution of condensed chromatin to the mechanical integrity of the nucleus and its ability to respond to extranuclear forces applied to the nuclear surface are difficult to reconcile with a liquid state. Two groups have recently studied the contribution of chromatin organization to mechanical stability of the nucleus. One found that the ability of the nucleus to resist an applied force was reduced approximately 10-fold by mildly digesting linker DNA and approximately 3-fold by treating cells with histone deacetylase inhibitors (Maeshima et al., 2018; Shimamoto et al., 2017), indicating that intact chromatin is needed to maintain the structural integrity of the nucleus. Stephens et al. (2019) further demonstrated that cells adapt to mechanical strain by activating mechanically sensitive ion channels, which stimulates the histone methylation machinery to drive assembly of more heterochromatin. The increased heterochromatinization of the nucleus resulted in increased resistance to externally applied stress (Stephens et al., 2019). These results demonstrate that nuclear chromatin is mechanically responsive and can resist significant applied force. This mechanical property is more consistent with a solid or gel state of bulk chromatin during interphase.

In this study, we critically assessed the mobility of defined nucleosomal arrays and native chromatin fragments in chromatin condensates that form *in vitro* under the conditions used by Maeshima et al. (2016b) and Gibson et al. (2019), together with directly evaluating the physical state of chromatin in living cells. When the properties of the condensates formed in $MgCl_2$-containing buffers were examined, we found that the packaged nucleosomal arrays were immobile, as in a solid- or gel-like state. Formation of liquid condensates could be induced by divalent cations, but only in the presence of DTT, BSA, and acetate anions. Under all other solution conditions examined, packaged nucleosomal arrays in condensates were constrained and solid-like. For our studies of chromatin *in vivo*, we incorporated fluorescent nucleotides into the genomic DNA of living cells, which enabled tracking of the mobility of the chromosomal DNA molecule rather than associated chromatin proteins. We found that DNA motion in heterochromatin and euchromatin domains was constrained so that it did not mix with surrounding chromatin even after hyperacetylation-induced decondensation. Finally, by evaluating constitutive heterochromatin at the pericentromere, we show that solid-like chromatin supports formation of liquid protein condensates *in vivo*. Our study provides concordant *in vitro* and *in vivo* results indicating that condensed chromatin is packaged into a solid- or gel-like state, supporting the concept of a globally constrained genome. Our results further demonstrate that solid chromatin formation is inherent to the nucleosomal array with no requirement for nonhistone chromatin proteins.

RESULTS

Condensed Chromatin *In Vitro* Is Intrinsically Packaged into a Solid-like State

In vitro, chromatin forms condensates under a wide range of salt conditions (Gibson et al., 2019; Hansen, 2002; Maeshima et al., 2016b; Perry and Chalkley, 1982). Chromatin in condensates is packaged as irregular 10-nm fibers that resemble chromatin packaging in chromosomes *in vivo* (Hansen et al., 2018; Maeshima et al., 2016b). In this study, we wanted to find out whether chromatin in condensates is mobile as in a liquid or constrained as in a solid. We first examined condensates formed by native chromatin fragments derived from micrococcal nuclease digestion, consisting of a heterogeneous population of nucleosomal arrays bound to H1 and a host of other chromatin-associated proteins. Consistent with a large body of published results (Hansen, 2002; Perry and Chalkley, 1982), native chromatin did not sediment appreciably in 100 mM NaCl but formed pelletable condensates in the presence of added $MgCl_2$ (Figure 1A). Fluorescence microscopy in 100 mM NaCl/2 mM $MgCl_2$ revealed the presence of individual chromatin condensates that were globular and ~0.5 μm in diameter and, upon contact, formed complex 3D structures rather than fusing into larger spheres (Figures 1B and 1C; Video S1). This size is smaller than that formed by nucleosomal arrays alone (Figure 1D) but consistent

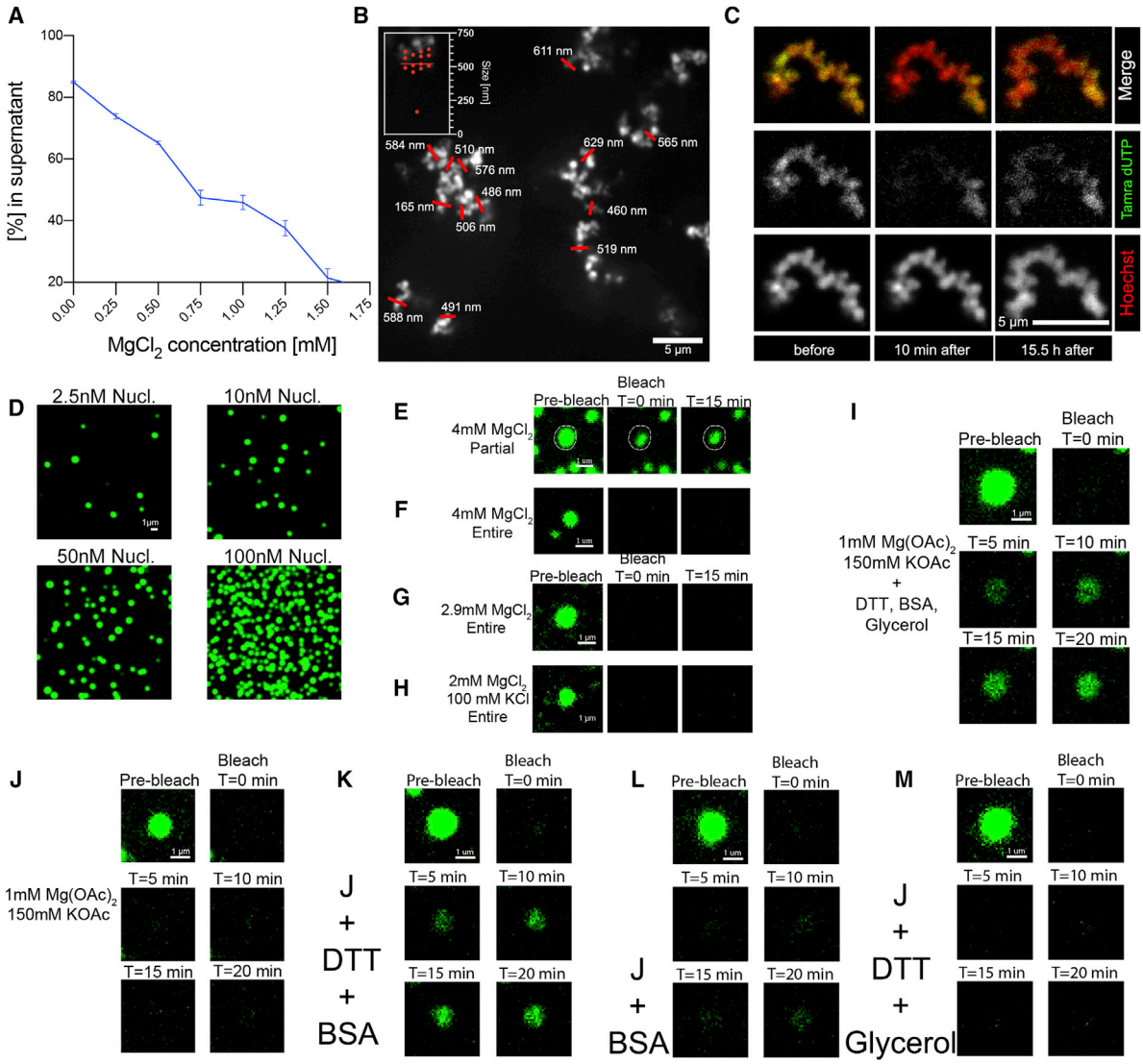

Figure 1. Solid-like Behavior of Chromatin Condensates *In Vitro*

(A) Formation of pelletable condensates by micrococcal nuclease-digested native chromatin of CH310T1/2 cells in the presence of 100 mM NaCl and increasing concentrations of magnesium was measured by recording the absorbance at 260 nm in solution following centrifugation to sediment the condensates.

(B) Native aggregated chromatin condensates formed in 5 mM $MgCl_2$ were stained with Hoechst and visualized by fluorescence deconvolution microscopy. Full-width half-maximum (FWHM) measurements of condensate diameters are shown.

(C) FRAP of native chromatin condensates stained with Hoechst and tetramethylrhodamine (TAMRA)-dUTP immediately after photobleaching, 30 min after photobleaching, and 24 h after photobleaching.

(D) Condensates formed in 4 mM $MgCl_2$ by Alexa 488-labeled 601–207 × 12 nucleosomal arrays were visualized by fluorescence microscopy. The total nucleosome concentration in the sample is indicated.

(E) Partial FRAP of a 601–207 × 12 condensate formed in 4 mM $MgCl_2$.

(F) FRAP of an entire 601–207 × 12 condensate formed in 4 mM MgCl2.

(G) FRAP of an entire 601–207 × 12 condensate formed in 2.9 mM $MgCl_2$. Approximately 15% of the nucleosomal arrays were unassociated in 2.9 mM $MgCl_2$ compared with 2% in 4 mM $MgCl_2$.

(H) FRAP of an entire 601–207 × 12 condensate formed in 2 mM $MgCl_2$/100 mM KCl.

(I) FRAP of an entire 601–207 × 12 condensate formed in 150 mM KOAc/1 mM $Mg[OAc]_2$ plus 5 mM DTT, 0.1 mg/mL BSA, and 5% glycerol.

(J) FRAP of an entire 601–207 × 12 condensate formed in 150 mM KOAc/1 mM $Mg[OAc]_2$ only.

(K) FRAP of an entire 601–207 × 12 condensate formed in 150 mM KOAc/1 mM $Mg[OAc]_2$ plus 5 mM DTT and 0.1 mg/mL BSA.

(L) FRAP of an entire 601–207 × 12 condensate formed in 150 mM KOAc/1 mM $Mg[OAc]_2$ plus 0.1 mg/mL BSA.

(M) FRAP of an entire 601–207 × 12 condensate formed in 150 mM KOAc/1 mM $Mg[OAc]_2$ plus 5 mM DTT and 5% glycerol.

with the smaller condensate sizes observed when histone H1 is bound to nucleosomal arrays (Maeshima et al., 2016b). When the condensates were subjected to fluorescence recovery after photobleaching (FRAP), we observed a lack of mixing of bleached and unbleached chromatin even after overnight incubation (Figure 1C). The findings that the chromatin condensates formed discrete pellets upon centrifugation (Figure 1A), did not fuse upon contact (Figure 1B), and did not mix after photobleaching (Figure 1C) indicate that native chromatin in condensates was packaged in a constrained solid-like state.

The solid-like properties of native chromatin condensates were unexpected considering recent descriptions of liquid chromatin condensates formed *in vitro* by arrays of positioned nucleosomes (Gibson et al., 2019). It is possible that the presence of H1 or other proteins in our native chromatin was responsible for this discrepancy. We therefore carefully reexamined salt-dependent condensate formation by model nucleosomal arrays. We utilized fluorescently labeled 12-mer 601 nucleosomal arrays with a 207-bp nucleosome repeat length (60-bp linkers) for these experiments. We first examined condensates formed in 4 mM $MgCl_2$, standard conditions used previously for structural analyses (Maeshima et al., 2016b). More than 95% of the nucleosomal arrays assemble into condensates that pellet in the microcentrifuge under these salt conditions (Maeshima et al., 2016b). The largest condensates formed under these conditions were globular and ranged from 0.5–1.0 μm (Figure 1D). Previous work has shown that ~1.0 μm is the maximum size reached by the condensates in $MgCl_2$, corresponding to structures that sediment at ~300,000 S (Maeshima et al., 2016b). The size distribution of the condensates in 5 mM $MgCl_2$, as determined by analytical ultracentrifugation, ranges from 35,000–300,000 S (~0.2–1.0 μm). Figure 1D shows that condensates formed in 4 mM $MgCl_2$ did not increase in maximum size with increasing chromatin concentration. At high concentrations, individual condensates formed networks of contacting 3D structures rather than fusing into larger globules, behavior inconsistent with a liquid state. We next determined the mobility of packaged nucleosomal arrays in condensates using FRAP. When a single condensate formed in 4 mM $MgCl_2$ was partially bleached, there was no mixing of unbleached and bleached arrays over a 15-min period (Figure 1E). No fluorescence recovery was observed when an entire condensate was bleached, regardless of whether the free array concentration in solution was very low (in 4 mM $MgCl_2$) or significantly higher (in 2.9 mM $MgCl_2$) (Figures 1F and 1G), indicating that there was no exchange between packaged nucleosomal arrays in condensates and unassociated nucleosomal arrays in solution. Finally, no recovery was observed for condensates formed in 100 mM KCl/2 mM $MgCl_2$ (Figure 1H), a similar condition used to characterize native chromatin condensates (Figures 1B and 1C). Collectively, the data in Figure 1 demonstrate that formation of chromatin condensates with solid-like properties in the presence of physiological concentrations of $MgCl_2$ and $MgCl_2$/KCl mixtures is an intrinsic property of arrays of nucleosomes. The condensates may be liquid-like during the initial stages of formation and become solid during the maturation process.

The observation of solid chromatin condensates differed from the results of Gibson et al. (2019), prompting us to assess what promoted liquid chromatin in their studies. We first characterized the condensates that form in 150 mM KOAc/1 mM $Mg[OAc]_2$ plus 5 mM DTT, 0.1 mg/ml BSA, and 5% glycerol, the conditions employed in their experiments (Gibson et al., 2019). Strikingly, when FRAP was performed on whole condensates formed under these conditions, we observed a linear increase in fluorescence recovery level over a 20-min period (Figure 1I; Figure S1A; Video S1). These results indicate that packaged nucleosomal arrays could diffuse in condensates as well as exchange with free nucleosomal arrays in solution, indicative of a liquid-like state of the chromatin. Given these findings, we systematically determined which component(s) of the buffers used by (Gibson et al. (2019)) were responsible for liquid-like behavior. In 150 mM KOAc/1 mM $Mg[OAc]_2$ buffers without added glycerol, DTT and BSA, there was no recovery after photobleaching of entire globules (Figure 1J; Video S1). Thus, liquid behavior of the condensates required one or more of the additives. In the presence of DTT and BSA, the chromatin remained in a liquid state, indicating that glycerol was not necessary for liquid behavior (Figure 1K; Video S1). When only BSA was present, negligible recovery (1%) was observed after 20 min (Figure 1L; Video S1). However, in the presence of BSA and DTT, recovery was much more substantial (Figure 1K; Video S1). Finally, when BSA was removed and only DTT and glycerol were added to the buffer, the condensates did not recover after photobleaching (Figure 1M; Video S1). Collectively, these results imply that maximum liquidity of the condensates requires reduced BSA in the buffer. Consistent with this conclusion, when the BSA was replaced with coronavirus disease 2019 (COVID-19) coat protein or glutathione S-transferase (GST) at the same molar concentration, there was no recovery of the condensates after photobleaching (Figures S1B and S1C), indicating that liquid behavior was not a non-specific consequence of high protein concentration. We therefore hypothesized that reduced BSA is sufficient to convert solid condensates to liquid condensates. However, when DTT and BSA were added to solutions containing 4 mM $MgCl_2$, the condensates did not recover after photobleaching (Figure S1D). Thus, liquid chromatin condensates were only observed under a single, highly specific set of conditions, requiring a combination of acetate anions, DTT, and BSA in addition to divalent cations. Under all other solution conditions tested, nucleosomal arrays in chromatin condensates were constrained and solid-like.

Replication Labeling Reveals Solid-like Behavior of Euchromatin and Heterochromatin in Living Cells, and Heterochromatin-Associated Proteins Exhibit Liquid-like Behavior

To ascertain whether condensed chromatin in the nucleus is a liquid, the extent of mixing in heterochromatin and euchromatin regions of mouse C3H/10T1/2 cells was determined. We first examined the properties of pericentric heterochromatin organized into chromocenters, which have been shown previously to be associated with membraneless compartments enriched in heterochromatin-associated proteins in *Drosophila* and murine embryonic fibroblasts (Strom et al., 2017). If the chromatin in the chromocenters is liquid, then photobleaching of labeled DNA would show evidence of diffusion of the label in the

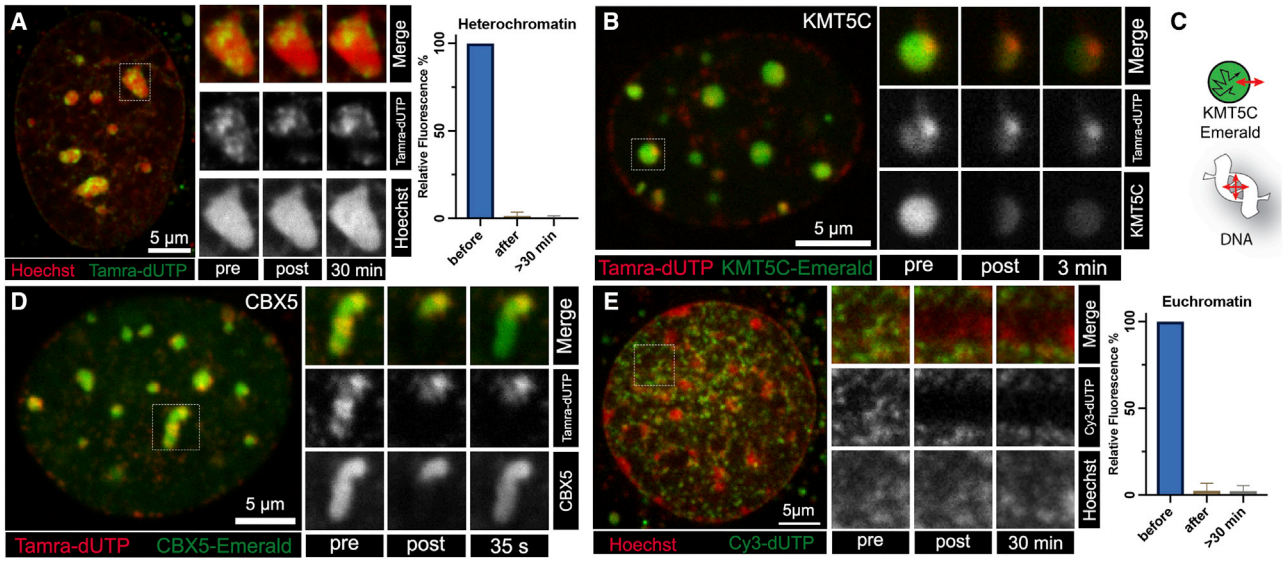

Figure 2. Solid-like Behavior of Heterochromatic and Euchromatic Chromatin in Living Cells

(A) A CH310T1/2 nucleus stained with Hoechst (red) for DNA and showing chromatin domains labeled with TAMRA-dUTP (green). Insets show the chromocenter (outlined by dashes on the left) before, immediately after, and 30 min after photobleaching. A plot of mean fluorescence before, after, and 30 min after photobleaching is shown (n = 15 from 3 separate experiments).

(B) Living CH310T1/2 nucleus replication labeled with TAMRA-dUTP (red) and transfected with KMT5C-Emerald (green). Insets show the chromocenter on the left outlined by dashes before, immediately after, and 30 min after photobleaching (separated by channels and merged).

(C) Schematic illustrating the immobility of DNA in the chromocenter and KMT5C-GFP mobility in the chromocenter and its inability to exchange with the surrounding nucleoplasm.

(D) Living CH310T1/2 nucleus replication-labeled with TAMRA-dUTP (red) and transfected with CBX5-Emerald HP1-alpha (green). Insets show the chromocenter on the left outlined with dashes before, immediately after, and 30 min after photobleaching (separated by channels and merged).

(E) A living CH310T1/2 nucleus stained with Hoechst (red) for DNA and showing chromatin domains labeled with TAMRA-dUTP (green). Insets show an area with multiple replication foci of early replicating (euchromatin) from the area on the left outlined by dashes before photobleaching, immediately after FRAP, and 30 min after photobleaching (separated by channels and merged). The graph shows fluorescence before, after, and 30 min after photobleaching.

Statistical analysis is shown in Table S1.

chromocenter. To test this, we pulse-labeled cells with a fluorescent nucleotide, TAMRA-dUTP, which was incorporated into the DNA (Schermelleh et al., 2001). When cells are pulse-labeled in S phase, they give distinctive labeling patterns related to temporal control of genome regulation. In early S phase, euchromatin replicates, and the labeled chromatin is seen as hundreds of individual foci scattered throughout the nucleoplasm (Ferreira et al., 1997) that are believed to correspond to single topologically associated domains (TADs) (Xiang et al., 2018). Following replication of euchromatin, the perinucleolar, perinuclear, and pericentric heterochromatin replicate. This enabled us to independently study cells that had incorporated label into heterochromatin or euchromatin. We imaged the cells 24–48 h after labeling. We observed that the individual chromocenters contained labeled and unlabeled regions of chromatin, indicating that there was no mixing of chromatin in chromocenters over long periods of time (Figure 2A). This is clearly distinct from the behavior of liquid condensates *in vitro*, where diffusion results in mixing of labeled and unlabeled macromolecules in the condensate (Hyman et al., 2014; Nakashima et al., 2019). To independently assess the physical state of chromatin in mouse chromocenters, we performed FRAP experiments. This is illustrated in Figure 2A and Video S2, which show an example where a line is photobleached to bisect several chromocenters, and then the labeled DNA is followed over time. Consistent with the lack of mixing of replication-labeled DNA, we found no recovery within the first 30 min after photobleaching (Figure 2A). This result indicates that, although the mouse chromocenters are near-spherical, the chromatin in chromocenters is not liquid-like under these conditions at the mesoscale.

As a control to test for liquidity in the nucleus, we examined two chromocenter-associated proteins that have been reported to be in a liquid state in the chromocenter. KMT5C, a histone H4 lysine 20 methyltransferase, shows liquid behavior in chromocenters but does not exchange with the nucleoplasm (Strickfaden et al., 2019). In contrast, CBX5, which can phase separate at high concentrations *in vitro* (Larson et al., 2017; Strom et al., 2017), was found to move rapidly into and out of mouse chromocenters (Erdel et al., 2020; Strom et al., 2017). We therefore performed two-channel FRAP experiments on TAMRA-dUTP-labeled cells transfected with fluorescent protein tags on KMT5C or CBX5 (Figures 2B and 2D). We found that KMT5C retains its liquid-like behavior in the chromocenter, as evidenced by the very slow but obvious recovery of KMT5C in the partially photobleached chromocenter (Figure 2B; Video S2; Figure S2A), and CBX5 exchanges rapidly with the nucleoplasm (Figure 2D; Video S2; Figure S2B). Despite observing the previously reported liquid-like behavior of these heterochromatin binding

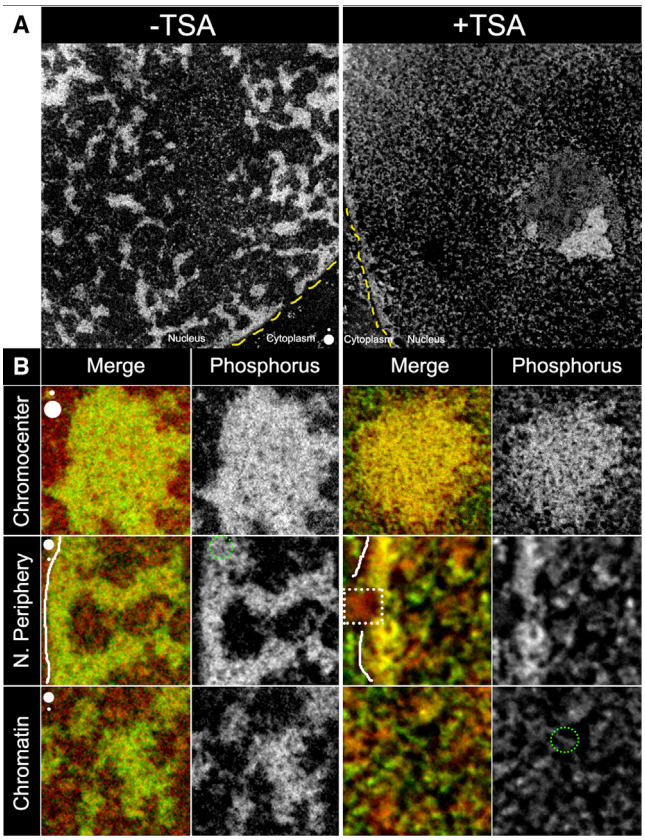

Figure 3. Histone Deacetylase Inhibition Results in Global Chromatin Decondensation

(A) Transmission electron microscopy images collected by ESI. Phosphorus elemental maps of 50-nm ultrathin sections show a nucleus of a C3H/10T1/2 cell (left) and a nucleus of a cell treated with 100 nM TSA for 24 h (right). The circles on the bottom right of the −TSA image are 30 nm and 100 nm in diameter. A portion of the cytoplasm is seen in both images (labeled cytoplasm), where ribosomes can be seen in the phosphorus maps. The dashed yellow lines indicate the boundary between the cytoplasm and the nucleus.

(B) ESI micrographs illustrating chromocenters, peripheral chromatin (N. Periphery), and nucleoplasmic chromatin (Chromatin) in the absence (left) and presence (right) of 24-h treatment with 100 nM TSA. The solid line in the N. Periphery color images indicate the position of the boundary between the nucleoplasm and cytoplasm. The position of a nuclear pore is highlighted by the dashed box. In the chromocenter images, circles represent diameters of 100 nm and 30 nm. In the bottom two rows, circles represent diameters of 30 nm and 10 nm. The green dashed circles highlight regions where individual chromatin fibers of approximately 10-nm diameter can be seen.

proteins, the underlying chromatin remains positionally stable and does not mix (Figures 2A, 2B, and 2D). These results indicate that DNA labeling does not cause a transition of the heterochromatin compartment to a solid state and demonstrates that the liquid-like behavior of heterochromatin proteins in chromocenters occurs amidst a solid scaffold of condensed chromatin (Figure 2C).

We also examined the physical state of euchromatic domains labeled during S phase. Cells labeled in early S phase incorporate labels into distinct small foci that may correspond to individual TADs (Xiang et al., 2018). We photobleached a region containing several individual foci and followed their fluorescence over time. As shown in Figure 2D and Video S2, fluorescence remains depleted over the time course of the experiment. Although the individual replication domains "jiggle" in space, there is no liquid-like mixing of the chromatin that can be observed. Quantification revealed negligible fluorescence immediately after and 30 min after photobleaching. This demonstrates that chromatin does not mix between individual euchromatic domains. We also examined whether this held independent of cell cycle. We found that G1-, S-, and G2-phase cells exhibited solid-like behavior in FRAP experiments (Figure S3A–S3C). The results shown in Figure 2 indicate that heterochromatin and euchromatin interphase domains in the nucleus exist in a solid-like state that precludes mixing with the surrounding nuclear environment, whereas specific protein components that associate with pericentric heterochromatin have liquid-like properties in solid domains.

Acetylation Decondenses Chromatin but Does Not Induce Liquid Behavior in Living Cells

Acetylation weakens but does not abolish the interactions of the core histone tails with DNA (Hong et al., 1993) and has been reported recently to promote mixing of microinjected nucleosomal arrays with nuclear chromatin (Gibson et al., 2019). Consequently, we next wanted to find out whether acetylation could transform solid-like chromatin into liquid chromatin *in vivo*. We treated cells with the histone deacetylase inhibitor Trichostatin A (TSA) to induce hyperacetylation of the histone tails to address this question. We first assessed the effect of TSA treatment on the structure of chromatin by direct visualization. Electron spectroscopic imaging (ESI) is a type of transmission electron microscopy that selectively enhances the contrast of phosphorus-rich structures such as chromatin (Hendzel et al., 1999). Using ESI, we determined the distribution of sizes of chromatin-dense structures in 50-nm-thick cross-sections of interphase nuclei. The images show phosphorus maps (grayscale) where the chromatin is visible, whereas the color maps show combined nitrogen (red) and phosphorus maps (green), resulting in yellow chromatin- and red protein-rich structures. For example, the nitrogen highlights non-chromatin structures, such as nuclear pores (dashed box in Figure 3B). To provide a sense of scale, circles of 10-, 30-, and 100-nm-diameter are shown. Under control conditions, condensed regions of chromatin can be observed in association with the lamina and in chromocenters. In addition, chromatin is found in condensed structures throughout the nuclear volume. Many of these domains are elongated condensed domains that are 100 nm or more in width, and they are generally irregular in shape in the 50-nm-thick section (Figure 3A, −TSA). At higher magnification (Figure 3B), these larger chromatin-dense structures have a fibrillar substructure where short sections of fibers of approximately 10 nm in diameter (ovals in Figure 3B) and consistently less than 30 nm in diameter can be observed to be packaged together to form approximately 100-nm-diameter chromatin-dense structures (Figure 3B, −TSA). In contrast, apart from chromocenters, the thin sections from cells treated with TSA reveal no obvious chromatin-dense structures throughout the nucleoplasm (Figures 3A and 3B, +TSA). Chromocenters persist under these conditions (Figure 3B,

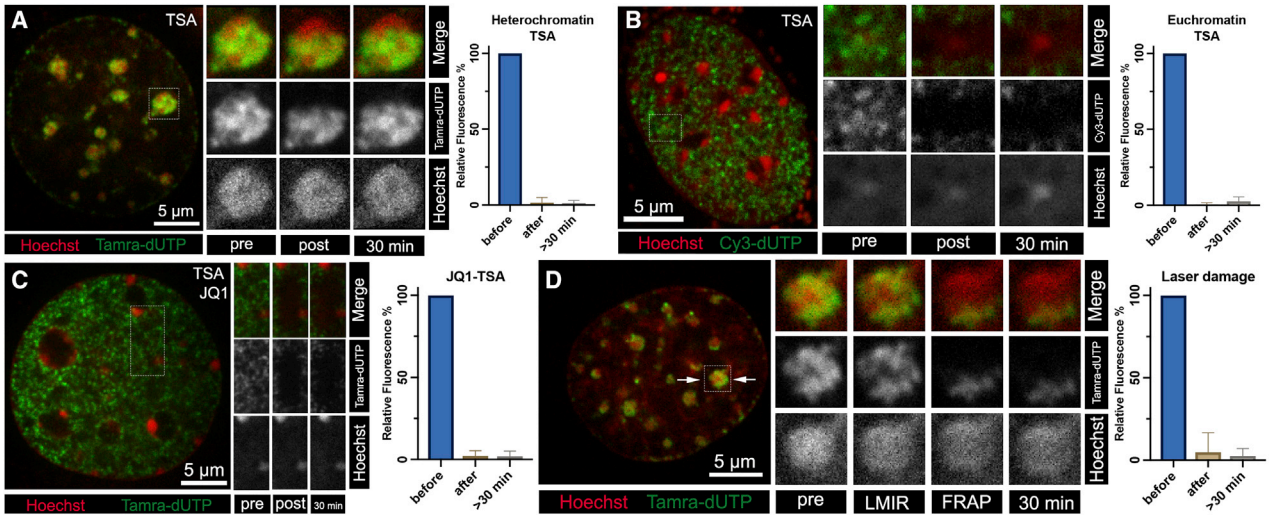

Figure 4. Solid-like Properties of Chromatin in the Presence of Treatments that Promote Dispersal of Condensed Intranuclear Chromatin

(A) A living C3H/10T1/2 nucleus treated with 100 nM TSA for 24 h, stained with Hoechst (red) for DNA, and showing chromatin domains labeled with TAMRA-dUTP (green). Insets of the chromocenter on the left outlined with dashes before, immediately after, and 30 min after photobleaching. The graph shows mean fluorescence before, after, and 30 min after photobleaching.

(B) A living CH310T1/2 nucleus treated with 100 nM TSA for 24 h, stained with Hoechst (red) for DNA, and showing chromatin domains labeled with TAMRA-dUTP (green). Insets of an area full of replication foci of mid-replicating (euchromatin) from the area on the left outlined by dashes before photobleaching, immediately after FRAP, and 30 min after photobleaching (separated by channels and merged). The graph shows mean fluorescence before, after, and 30 min after photobleaching.

(C) Photobleaching of a nucleus of a C3H/10T1/2 cell treated with 100 nM TSA and 2 mM of the bromodomain inhibitor JQ-1. Replication domains still visible as distinct entities were photobleached. A magnified area full of mid-replicating replication foci (euchromatin) on the left outlined with dashes before photobleaching (separated by channels and merged), immediately after FRAP, and 30 min after photobleaching show that the bleached replication domains are not recovering. The graph shows mean fluorescence before, after, and 30 min after photobleaching.

(D) Left: image of a C3H/10T1/2 cell being microirradiated by a 405-nm laser for laser damage induction bisecting a chromocenter (arrows). Right: magnified chromocenter on the left outlined by dashes before laser micro-irradiation, immediately after, after photobleaching, and 30 min after showing that the bleached replication domains are not recovering (separated by channels and merged). The graphs show mean fluorescence before, after, and 30 min after photobleaching. Statistical analysis is shown in Table S1.

chromocenters +TSA), and there may be some retention of higher-density chromatin associated with the nuclear lamina (Figures 3A, +TSA, and 3B, periphery +TSA), but, in general, the chromatin signal is largely punctate (Figures 3A and 3B), reflecting dispersal of the dense, ~100-nm chromatin structures found throughout the nucleoplasm. These results establish that classic heterochromatin structures associated with the nuclear lamina and chromocenters show some persistence upon histone hyperacetylation. In contrast, the condensed chromatin found outside of the classic heterochromatin structures is mostly disassembled upon TSA treatment.

Having established that, in the presence of TSA, there is minimal dense chromatin formation in the nucleoplasm outside of chromocenters, we assessed the properties of the hyperacetylated chromatin using time-lapse microscopy and FRAP. After TSA treatment, the chromocenters persisted (Figure 4A), as expected from the transmission electron microscopy data. Interestingly, despite the observed disassembly of the condensed chromatin found throughout the nucleoplasm, in cells where euchromatin incorporated the label during the pulse, the labeled chromatin still persisted as numerous independently visible foci (Figure 4B). When these foci were subjected to FRAP, negligible recovery of the bleached regions occurred over a 30-min period (Figures 4A and 4B; Video S3). In this instance, although recovery was near zero, the measured intensity did show a small but statistically significant increase at the 30-min time point. Although we cannot rule out that acetylated chromatin is able to undergo slow and limited mixing, even fixed specimens show slight differences in intensity (Figure S3D). This reflects small changes in z-positioning because of thermal fluctuations. In the case of living cells, the other dynamics taking place over the course of 30 min in a living cell are more likely the basis of these small changes in fluorescence.

Although we did not observe clear evidence of liquidity, we did observe motion. The individual foci, which represent regions of chromatin that have incorporated the label at the time of the pulse and may be individual TADs (Xiang et al., 2018), were able to move in x, y, and z directions to a limited extent (Video S3). The individual foci that were fully bleached did not recover significant amounts of fluorescence (Figure 4B), indicating that chromatin does not readily mix between unbleached and partially bleached foci. Moreover, although these individual foci show some motion, the failure of the photobleached region to be repopulated by non-photobleached foci surrounding the photobleached region indicates how restricted the motion of this dispersed chromatin is in living cells. These data are inconsistent with acetylation driving chromatin into a liquid state in cells, as reported by Gibson et al. (2019), where the short acetylated

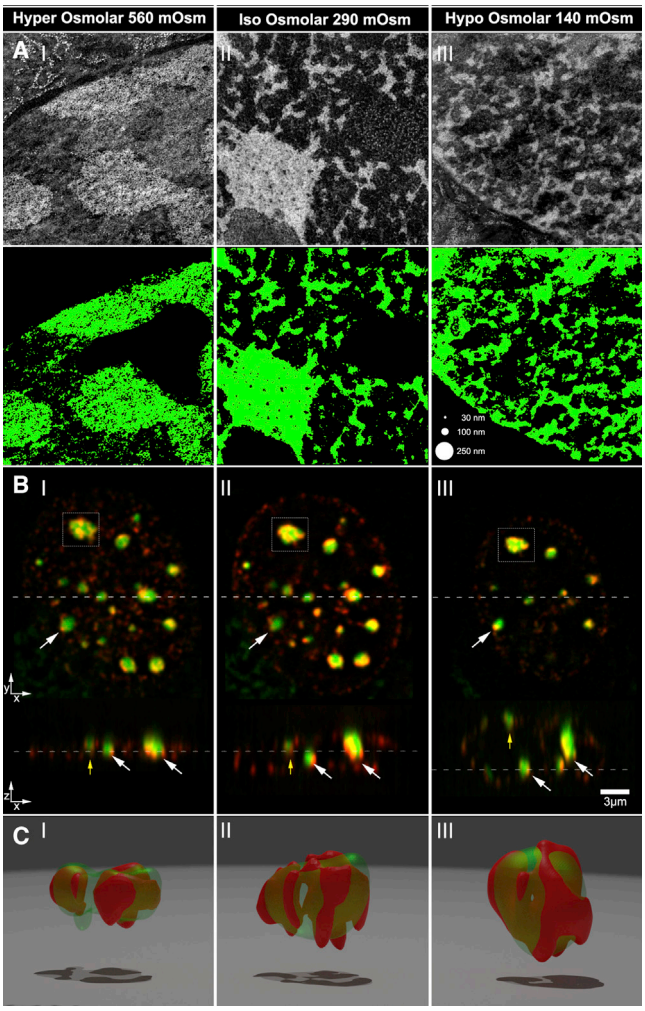

Figure 5. The Sensitivity of Condensed Chromatin to Changing Ionic Conditions in Living Cells

(A) Transmission electron microscopy images showing phosphorus maps recorded by ESI of C3H/10T1/2 nuclei (top) and a binary illustration of chromatin content (bottom) in cells exposed to different osmotic environments (I, hyperosmolar, 560 mOsm; II, iso-osmolar, 290 mOsm; III, hypo-osmolar, 140 mOsm).

(B) The relative orientation of replication-labeled chromatin domains remains stable irrespective of changes in the osmotic environment. The nucleus of a C3H/10T1/2 nucleus replication labeled by TAMRA-dUTP (red) and KMT5C-GFP (green) and exposed to different osmotic environments (I, 140 mOsm; II, 290 mOsm; III, 560 mOsm) is shown in an x-y (top) and a y-z (bottom) cross-section. The dashed line indicates the cutting plane representing the y-z projection. Arrows point to corresponding replication domains in the x-y and y-z projections.

(C) 3D reconstructions of the chromocenter, outlined by dashes in the top part.

nucleosomal arrays mixed readily and dispersed in the nucleoplasm. Rather, our results indicate additional constraints on endogenous acetylated chromatin that may not apply to the short microinjected arrays examined by Gibson et al. (2019).

One explanation for the failure of dispersed acetylated chromatin to mix is that it becomes immobilized by association with bromodomain (BRD)-containing proteins, which have been shown to undergo liquid unmixing in cells and bind to superenhancers (Sabari et al., 2018). It has been demonstrated recently that acetylated chromatin is dispersed in solution but can undergo liquid demixing in the presence of bromodomain-containing proteins (Gibson et al., 2019). This bromodomain-mediated phase separation was inhibited by JQ1, an inhibitor of BRD-acetylated lysine interactions. Consequently, we tested whether treating cells with JQ1 would enable hyperacetylated chromatin to adopt liquid-like behavior. We found that JQ1 had no effect on the inability of hyperacetylated chromatin to undergo mixing in FRAP experiments—the photobleached regions persisted throughout the time course (Figure 4C; Video S3).

To further test whether dispersing chromatin can establish a liquid state, we induced chromatin decondensation through laser micro-irradiation. This results in very rapid poly(ADP-ribosyl)ation (PARP)-dependent decondensation of chromatin in living cells (Strickfaden et al., 2016) and is evident by the increase in diameter and dilution of fluorescence of Hoechst-contrasted chromatin (Figure 4D). When replication-labeled chromatin was photobleached simultaneously with laser micro-irradiation, we again did not observe mixing of the chromatin (Figure 4D; Video S3). When we damaged a region containing early S phase replicated foci and tracked these foci, we found that the chromatin expanded laterally in an isometric fashion and displaced, rather than mixed with, chromatin outside of the damaged region (Figure S4; Video S4). Thus, despite the ability of laser micro-irradiation and histone hyperacetylation to decondense and disperse native chromatin in the nucleus, they do not promote liquid-like behavior (i.e., mixing) of labeled chromatin in living cells. These results indicate that, even when fiber-fiber contacts are not obvious in thin sections of interphase nuclei, there are sufficient nucleosome-nucleosome interactions to prevent mixing (liquid-like) behavior at the mesoscale.

The Effect of Osmolarity on Intranuclear Chromatin Organization

The expansion of chromatin following chromatin decondensation by poly(ADP-ribosyl)ation prompted us to further explore the responsiveness of chromatin structure to changes in the ion concentrations in the intracellular environment. We assessed the changes in the organization of individual chromatin fibers by transmission electron microscopy following exposure of cells to hyperosmotic conditions, which increase intracellular ion concentrations and molecular crowding, and hypoosmotic conditions, which decrease both. Figure 5A shows that hyperosmotic treatment induced profound ultrastructural changes of chromatin. In the corresponding binary image maps, green indicates the positions of regions of chromatin. The ~100-nm-diameter dense chromatin structures are no longer found throughout the nucleoplasm. Instead, chromatin accumulates in structures that are much larger than what is normally found in the nucleoplasm. Figure 5B shows a single cell nucleus followed through changes in osmolarity. Hyperosmolar treatment results in a marked decrease in nuclear volume, whereas hypo-osmolar treatment results in rapid expansion of the nuclear volume (Figures 5B; Figure S4). A single chromocenter is illustrated as a surface-rendered projection in Figure 5C. This reveals that, although the volume is altered significantly, the relative

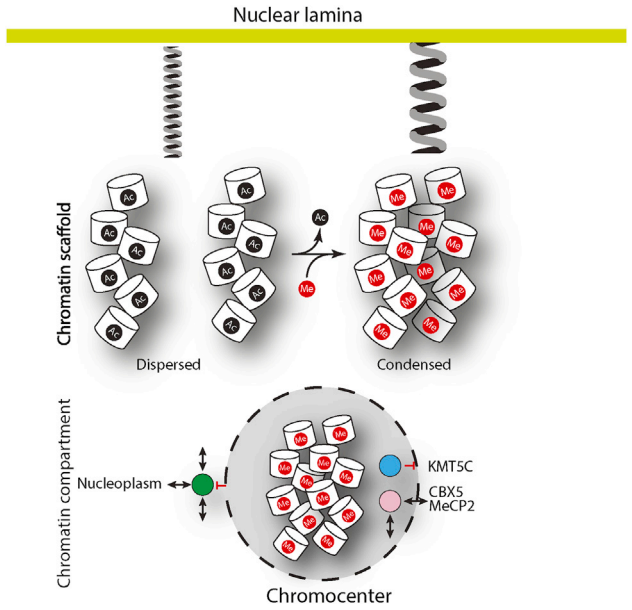

Figure 6. A Model to Explain the Physical Properties of Chromatin and Chromatin Compartments

Chromatin exists in two physical states: dispersed and condensed. Internucleosomal interactions are disrupted by acetylation, whereas condensed states are associated with specific histone methylations (H3 lysine 9 methylation, H3 lysine 27 methylation, and H4 K20 methylation). In the dispersed state, residual internucleosomal/interfiber interactions provide low mechanical resistance to extracellular and extranuclear forces. In the condensed state, more frequent internucleosomal and interfiber interactions provide greater resistance to applied force and contribute to the mechanical integrity of the nucleus. Histone modifications are concentrated through nucleosome-nucleosome and fiber-fiber interactions that package chromatin at higher densities. This increases the concentration of modification-specific histone binding proteins above the threshold for LLPS, and a liquid compartment is formed that may filter molecules (black spheres) that enter from the nucleoplasm and provide an energy barrier to nucleoplasmic release from resident client proteins such as KMT5C.

geometric orientation of replication-labeled chromatin remained unchanged in individual chromocenters across these three conditions (Figure 5B). Although condensates that form by LLPS usually show sensitivity toward osmotic changes of the surrounding environment (Olins et al., 2020), the contraction and expansion behavior of the chromatin domains in this experiment resembled that of a hydrogel, not that of a liquid.

DISCUSSION

Interphase chromosomes exist as discrete territories that reflect short- and long-range interactions primarily in the same chromatin fiber (Cremer and Cremer, 2001; Cremer et al., 2020; Lieberman-Aiden et al., 2009). In this manner, self-interaction of the chromatin fiber across different length scales helps mold and maintain interphase chromosome structure. When assessed *in vitro* using short nucleosomal arrays, chromatin self-interaction leads to formation of globular condensates with diameters in the micron range (Gibson et al., 2019; Maeshima et al., 2016b). Packaging of nucleosomal arrays in chromatin condensates is thought to recapitulate long-range chromatin interactions in chromosomes *in vivo* (Hansen et al., 2018; Maeshima et al., 2016b) but the physical state(s) imparted by these interactions are poorly understood. Here we demonstrate that the condensates formed by native chromatin fragments in $MgCl_2$/NaCl mixtures are solid-like (Figures 1B and 1C). In addition, we found that condensates formed by positioned nucleosomal arrays have solid-like properties under all solution conditions examined (Figures 1D–1H), with one exception. In magnesium acetate with added BSA and DTT, nucleosomal arrays assemble into condensates with liquid-like properties (Figures 1I and 1K), as reported by Gibson et al. (2019). These results demonstrate that nucleosomal arrays have an intrinsic capacity to condense into solid-like structures without any requirement for the chromatin binding proteins that help define specialized chromatin domains such as chromocenters. Given that each nucleosome tightly binds ~3,000 water molecules (Davey et al., 2002), the solid-like state of condensed chromatin may be a hydrogel.

LLPS has been used to explain multiple aspects of chromatin structure and function in cells (Erdel and Rippe, 2018; Gibson et al., 2019; Larson et al., 2017; Maeshima et al., 2016a; Narlikar, 2020; Sanulli et al., 2019; Strom et al., 2017; Wang et al., 2019). Most notably, rather than chromatin condensation being driven by mechanisms inherent to the nucleosome, liquid-liquid unmixing of chromatin-bound proteins has been proposed to initiate formation of phase-separated heterochromatin compartments. This model is based on the recently identified propensity of free CBX5 and CBX2 to phase separate at low micromolar concentrations and predicts that heterochromatin structures may be liquid in cells. We tested the liquidity of chromatin in living cells by incorporating a fluorescent nucleotide directly into the DNA. This enabled us to study mixing of chromatin itself rather than the proteins that transiently bind to it. We found the physical state of chromatin *in vivo* to be a solid on the timescale of minutes to hours, which is a relevant timescale for functional regulation of the genome in a dividing cell. We established this by assessing the physical state of packaged chromatin in living cells labeled using fluorescent nucleotides and found no evidence of mixing of surrounding chromatin. This applied to the euchromatin (Figures 2D and 4B) and heterochromatin (Figures 2 and 4) compartments and in response to multiple stimuli that induced chromatin dispersion or decompaction, where chromatin appeared to disperse evenly to produce solid-like assemblies with decreased fiber density (Figures 4 and 5). Thus, we could not find conditions that promoted the mixing observed with a liquid chromatin state.

It is important to recognize that the solid-like behavior of chromatin we observe *in vitro* and in living cells is measured at the mesoscale (10–1,000 nm). This scale is relevant to the material properties of the cell nucleus and organization of chromosomes into territories and of chromatin into compartments. Although there is ample evidence of constrained diffusion of chromatin (Maeshima et al., 2020), demonstrating that chromatin is liquid requires evidence that nucleosomes can move in the domain. We did not find evidence of this at mesoscale resolutions. However, double-label experiments where single nucleosomes and early S-phase replication domains (putative individual TADs)

are co-tracked reveal that nucleosomes can show nanoscale liquidity that reflects movement in the domain (Nozaki et al., 2017). We expect that this is essential for chromatin to function. The available data indicate that condensed chromatin may be liquid-like at the nanoscale but is solid-like at the mesoscale.

Mechanistically, why does condensed chromatin exist as a solid? By its very nature, chromatin is a multivalent polymer that consists of intrinsically disordered core histone tails that project from the surface of each nucleosome to support a range of molecular interactions. It has long been known that Mg^{2+} dependent assembly of chromatin condensates requires the histone tail domains (Gordon et al., 2005; Schwarz et al., 1996), which act additively and independently to mediate condensate formation (Gordon et al., 2005; Schwarz et al., 1996). In condensates, the tails interact with DNA of their own and other arrays (Kan et al., 2009; Kan et al., 2007). Importantly, tail-DNA interactions are not weak; the equilibrium constant for an H4 tail peptide binding to DNA is 5×10^{11} M^{-1} (Hong et al., 1993). Given that there are hundreds of thousands of nucleosomes within a 1.0-μm diameter chromatin condensate (Maeshima et al., 2016b), we expect the magnitude of summed strong tail-DNA interactions to constrain the nucleosomes into a solid state. Small-angle X-ray scattering studies suggest that there may be local mobility of nucleosomes in solid condensates that is antagonized by binding of histone H1 (Maeshima et al., 2016b). Thus, although chromatin may show liquid-like behavior at the nanoscale because of local dissociation or disruption of tail-DNA interactions, the sum of all nucleosomal contacts in condensed chromatin results in solid-like behavior at the mesoscale.

Our experiments show that high concentrations of reduced BSA and acetate anions are required to produce chromatin condensates that are liquid on the mesoscale *in vitro*. For this to occur, we envision that tail-DNA interactions must persist but become very weak so that they are fluctuating rather than stable. Upon reduction, BSA forms a molten globule state characterized by increased surface hydrophobicity (Lee and Hirose, 1992). It is possible that, in addition to electrostatic contacts with DNA phosphates, the tails make hydrophobic contacts with DNA bases that are disrupted by reduced BSA. High concentrations of acetate anions presumably weaken the electrostatic interactions by competing for tail binding to DNA phosphates. Collectively, these two effects may cause tail-DNA interactions to be dynamic, resulting in a liquid chromatin state. If there are *in vivo* conditions that can mimic the *in vitro* effects of reduced BSA and acetate anions, any given specific region of chromatin in the nucleus could be converted to a liquid state, although it is clear from our *in vivo* experiments that such conditions do not exist in bulk throughout the nucleus.

Although we did not observe evidence of liquid behavior of euchromatin labeled in early S phase (Figure 2E) or in cells where chromatin has been dispersed by TSA (Figures 4B and 4C), we did observe relative movement of individual S-phase labeled euchromatic foci relative to each other (Video S3). This relative movement has been reported before (Xiang et al., 2018). It is important to recognize that mobility is not evidence of liquidity. Liquidity requires evidence of chromatin mixing. There is considerable evidence that individual gene loci undergo constrained diffusion (Chubb et al., 2002; Gasser, 2002; Marshall et al., 1997) and active transport (Chuang and Belmont, 2007; Dundr et al., 2007; Khanna et al., 2014). Rather than liquidity, this most likely reflects the viscoelastic properties of the chromatin solid observed in mechanical studies (see below; Maeshima et al., 2018; Stephens et al., 2017, 2019). Given that each early S-phase replication-labeled focus appears to correspond to an individual TAD (Xiang et al., 2018), the observed motions of gene loci would most easily be explained by flexibility and elasticity of the decondensed nucleosomal chain in regions that link individual TADs, as suggested previously (Xiang et al., 2018). Thus, as is the case *in vitro* (see above), there is evidence of chromatin liquidity *in vivo* at the nanoscale, whereas condensed chromatin structures that form in interphase nuclei have solid-like properties that emerge from the summed interactions of individual nucleosomes in the chromatin-dense environment.

The solid state of chromatin in the nucleus has several advantages. It provides mechanical stability to the genome and the cell itself, as revealed by the ability of cells to adapt to an applied force by increasing rigidity through heterochromatin formation (Stephens et al., 2019). The reduction in rigidity by histone acetylation (Maeshima et al., 2018) suggests that histone post-translational modifications can modulate the viscoelastic properties of a chromatin gel without transition to a liquid state. Consistent with this observation, our electron microscopy analyses revealed that the partial disassembly of condensed chromatin regions induced by histone acetylation was associated with reduced fiber-fiber interactions (Figure 3) but did not alter the solid-like behavior (Figures 4B and 4C). Second, self-association of chromatin results in higher local concentrations of the histone modifications that decorate the chromatin. Proteins that bind to these modifications will concentrate in these regions, and many of them have been shown to undergo LLPS at micromolar concentrations. Moreover, mixing nucleosomal arrays with CBX2 decreases the critical concentration of CBX2 required for LLPS and liquid droplet formation (Plys et al., 2019). Similarly, MeCP2 is only able to form droplets in the presence of DNA or chromatin (Wang et al., 2020). Models derived from studying phase separation of heterochromatin proteins envision heterochromatin proteins initiating condensation of chromatin (Larson et al., 2017; Plys et al., 2019; Strom et al., 2017; Tatavosian et al., 2019; Wang et al., 2020). However, chromocenters are formed shortly after mitosis and, hence, are initiated from a state where chromatin density is highest. Thus, it is more likely that condensed chromatin provides a nucleation site for LLPS of heterochromatin binding proteins rather than LLPS of heterochromatin binding proteins driving condensation. By reducing the critical concentration needed for LLPS and/or elevating local protein concentrations through binding and retention of chromatin binding proteins capable of LLPS, solid chromatin provides a scaffold that promotes formation of phase-separated compartments in the nucleoplasm. We therefore propose that chromatin has an intrinsic ability to form an elastic, solid, cross-linked network of chromatin that provides mechanical strength to the interphase nucleus and contributes to spatial organization of the nucleoplasm by concentrating binding sites for chromatin binding proteins that themselves undergo liquid unmixing (Figure 6).

STAR★METHODS

Detailed methods are provided in the online version of this paper and include the following:

- KEY RESOURCES TABLE
- RESOURCE AVAILABILITY
  - Lead Contact
  - Materials Availability
  - Data and Code Availability
- EXPERIMENTAL MODEL AND SUBJECT DETAILS
- METHOD DETAILS
  - Fluorescently labeled dUTPs
  - Preparation of chromatin fragments from cell nuclei and differential centrifugation assay for chromatin condensate formation
  - Saponin labeling
  - Scratch labeling
  - Inhibitor treatment
  - Transfection
  - Assembly and Purification of unlabeled recombinant histone octamers
  - Alexa 488 H4 E63C labeling and labeled histone octamer assembly
  - Purification of 601-207bp x 12 template DNA
  - Assembly of Alexa 488 labeled nucleosomal arrays
  - Chromatin condensate formation
  - Fluorescence microscopy and FRAP
  - Assembly of Alexa 488 Labeled Nucleosomal Arrays
  - Chromatin condensate formation and Fluorescence Microscopy/photobleaching
  - Fixation of cells
  - Fluorescence microscopy (Fractionated Chromatin/in-vivo)
  - Hyper- and Hypotonic treatment of cells
  - Electron Spectroscopic Imaging
  - Test for DNA damage by nucleotide incorporation
- QUANTIFICATION AND STATISTICAL ANALYSIS
  - Data processing
  - Image Processing for Figure Creation

SUPPLEMENTAL INFORMATION

Supplemental Information can be found online at https://doi.org/10.1016/j.cell.2020.11.027.

ACKNOWLEDGMENTS

We would like to note the initial independent development of nucleosomal array studies by T.O.T. We thank Dr. Armin Gamper for providing JQ1 and Dr. Xuejun Sun and the Cell Imaging Facility for microscopy support. We also thank Darin McDonald and Kristal Missiaen for technical support and Thomas Cremer for discussions and support. A.S., D.A.U., H.S., and M.J.H. would like to dedicate their contribution to this work to the memory of Darin McDonald, who died suddenly during the completion of the study. This work was supported by grants from the National Science Foundation (MCB-1814012 to J.C.H.), the Canadian Institutes of Health Research (CIHR PS 162153 to M.J.H.), and the Cancer Research Society (CRSDI 368 2018 OG 23446 to D.A.U. and M.J.H.).

AUTHOR CONTRIBUTIONS

The *in vitro* chromatin condensation experiments with nucleosomal arrays were designed by T.O.T. and J.C.H. and executed by T.O.T. All other experiments were designed by H.S. and M.J.H. and executed by H.S., with the exception of the *in vitro* condensation experiments with endogenous chromatin, which were designed by M.J.H. and A.S. and executed by A.S and H.S., and the CBX5 and KMT5C experiments, which were designed by D.A.U. and H.S. and executed by H.S. The manuscript was written by H.S., T.O.T., J.C.H., and M.J.H. All authors contributed to manuscript editing.

DECLARATION OF INTERESTS

The authors declare no competing interests.

Received: June 26, 2020
Revised: September 16, 2020
Accepted: November 16, 2020
Published: December 15, 2020

REFERENCES

Albiez, H., Cremer, M., Tiberi, C., Vecchio, L., Schermelleh, L., Dittrich, S., Küpper, K., Joffe, B., Thormeyer, T., von Hase, J., et al. (2006). Chromatin domains and the interchromatin compartment form structurally defined and functionally interacting nuclear networks. Chromosome Res. *14*, 707–733.

Bian, Q., and Belmont, A.S. (2012). Revisiting higher-order and large-scale chromatin organization. Curr. Opin. Cell Biol. *24*, 359–366.

Chuang, C.H., and Belmont, A.S. (2007). Moving chromatin within the interphase nucleus-controlled transitions? Semin. Cell Dev. Biol. *18*, 698–706.

Chubb, J.R., Boyle, S., Perry, P., and Bickmore, W.A. (2002). Chromatin motion is constrained by association with nuclear compartments in human cells. Curr. Biol. *12*, 439–445.

Cremer, T., and Cremer, C. (2001). Chromosome territories, nuclear architecture and gene regulation in mammalian cells. Nat. Rev. Genet. *2*, 292–301.

Cremer, T., Cremer, M., Hübner, B., Silahtaroglu, A., Hendzel, M., Lanctôt, C., Strickfaden, H., and Cremer, C. (2020). The Interchromatin Compartment Participates in the Structural and Functional Organization of the Cell Nucleus. BioEssays *42*, e1900132.

Davey, C.A., Sargent, D.F., Luger, K., Maeder, A.W., and Richmond, T.J. (2002). Solvent mediated interactions in the structure of the nucleosome core particle at 1.9 a resolution. J. Mol. Biol. *319*, 1097–1113.

Dundr, M., Ospina, J.K., Sung, M.H., John, S., Upender, M., Ried, T., Hager, G.L., and Matera, A.G. (2007). Actin-dependent intranuclear repositioning of an active gene locus in vivo. J. Cell Biol. *179*, 1095–1103.

Eltsov, M., Maclellan, K.M., Maeshima, K., Frangakis, A.S., and Dubochet, J. (2008). Analysis of cryo-electron microscopy images does not support the existence of 30-nm chromatin fibers in mitotic chromosomes in situ. Proc. Natl. Acad. Sci. USA *105*, 19732–19737.

Erdel, F., and Rippe, K. (2018). Formation of Chromatin Subcompartments by Phase Separation. Biophys. J. *114*, 2262–2270.

Erdel, F., Rademacher, A., Vlijm, R., Tunnermann, J., Frank, L., Weinmann, R., Schweigert, E., Yserentant, K., Hummert, J., Bauer, C., et al. (2020). Mouse Heterochromatin Adopts Digital Compaction States without Showing Hallmarks of HP1-Driven Liquid-Liquid Phase Separation. Mol. Cell *78*, 236–249.e7.

Ferreira, J., Paolella, G., Ramos, C., and Lamond, A.I. (1997). Spatial organization of large-scale chromatin domains in the nucleus: a magnified view of single chromosome territories. J. Cell Biol. *139*, 1597–1610.

Finch, J.T., and Klug, A. (1976). Solenoidal model for superstructure in chromatin. Proc. Natl. Acad. Sci. USA *73*, 1897–1901.

Fussner, E., Ching, R.W., and Bazett-Jones, D.P. (2011). Living without 30nm chromatin fibers. Trends Biochem. Sci. *36*, 1–6.

Fussner, E., Strauss, M., Djuric, U., Li, R., Ahmed, K., Hart, M., Ellis, J., and Bazett-Jones, D.P. (2012). Open and closed domains in the mouse genome are configured as 10-nm chromatin fibres. EMBO Rep. *13*, 992–996.

Gasser, S.M. (2002). Visualizing chromatin dynamics in interphase nuclei. Science *296*, 1412–1416.

Gibson, B.A., Doolittle, L.K., Schneider, M.W.G., Jensen, L.E., Gamarra, N., Henry, L., Gerlich, D.W., Redding, S., and Rosen, M.K. (2019). Organization of Chromatin by Intrinsic and Regulated Phase Separation. Cell *179*, 470–484.e21.

Gordon, F., Luger, K., and Hansen, J.C. (2005). The core histone N-terminal tail domains function independently and additively during salt-dependent oligomerization of nucleosomal arrays. J. Biol. Chem. *280*, 33701–33706.

Hansen, J.C. (2002). Conformational dynamics of the chromatin fiber in solution: determinants, mechanisms, and functions. Annu. Rev. Biophys. Biomol. Struct. *31*, 361–392.

Hansen, J.C., Connolly, M., McDonald, C.J., Pan, A., Pryamkova, A., Ray, K., Seidel, E., Tamura, S., Rogge, R., and Maeshima, K. (2018). The 10-nm chromatin fiber and its relationship to interphase chromosome organization. Biochem. Soc. Trans. *46*, 67–76.

Hendzel, M.J., Boisvert, F., and Bazett-Jones, D.P. (1999). Direct visualization of a protein nuclear architecture. Mol. Biol. Cell *10*, 2051–2062.

Hong, L., Schroth, G.P., Matthews, H.R., Yau, P., and Bradbury, E.M. (1993). Studies of the DNA binding properties of histone H4 amino terminus. Thermal denaturation studies reveal that acetylation markedly reduces the binding constant of the H4 "tail" to DNA. J. Biol. Chem. *268*, 305–314.

Hyman, A.A., Weber, C.A., and Jülicher, F. (2014). Liquid-liquid phase separation in biology. Annu. Rev. Cell Dev. Biol. *30*, 39–58.

Joti, Y., Hikima, T., Nishino, Y., Kamada, F., Hihara, S., Takata, H., Ishikawa, T., and Maeshima, K. (2012). Chromosomes without a 30-nm chromatin fiber. Nucleus *3*, 404–410.

Kan, P.Y., Lu, X., Hansen, J.C., and Hayes, J.J. (2007). The H3 tail domain participates in multiple interactions during folding and self-association of nucleosome arrays. Mol. Cell. Biol. *27*, 2084–2091.

Kan, P.Y., Caterino, T.L., and Hayes, J.J. (2009). The H4 tail domain participates in intra- and internucleosome interactions with protein and DNA during folding and oligomerization of nucleosome arrays. Mol. Cell. Biol. *29*, 538–546.

Khanna, N., Hu, Y., and Belmont, A.S. (2014). HSP70 transgene directed motion to nuclear speckles facilitates heat shock activation. Curr. Biol. *24*, 1138–1144.

Larson, A.G., Elnatan, D., Keenen, M.M., Trnka, M.J., Johnston, J.B., Burlingame, A.L., Agard, D.A., Redding, S., and Narlikar, G.J. (2017). Liquid droplet formation by HP1α suggests a role for phase separation in heterochromatin. Nature *547*, 236–240.

Lee, J.Y., and Hirose, M. (1992). Partially folded state of the disulfide-reduced form of human serum albumin as an intermediate for reversible denaturation. J. Biol. Chem. *267*, 14753–14758.

Lieberman-Aiden, E., van Berkum, N.L., Williams, L., Imakaev, M., Ragoczy, T., Telling, A., Amit, I., Lajoie, B.R., Sabo, P.J., Dorschner, M.O., et al. (2009). Comprehensive mapping of long-range interactions reveals folding principles of the human genome. Science *326*, 289–293.

Maeshima, K., Hihara, S., and Eltsov, M. (2010a). Chromatin structure: does the 30-nm fibre exist in vivo? Curr. Opin. Cell Biol. *22*, 291–297.

Maeshima, K., Hihara, S., and Takata, H. (2010b). New insight into the mitotic chromosome structure: irregular folding of nucleosome fibers without 30-nm chromatin structure. Cold Spring Harb. Symp. Quant. Biol. *75*, 439–444.

Maeshima, K., Ide, S., Hibino, K., and Sasai, M. (2016a). Liquid-like behavior of chromatin. Curr. Opin. Genet. Dev. *37*, 36–45.

Maeshima, K., Rogge, R., Tamura, S., Joti, Y., Hikima, T., Szerlong, H., Krause, C., Herman, J., Seidel, E., DeLuca, J., et al. (2016b). Nucleosomal arrays self-assemble into supramolecular globular structures lacking 30-nm fibers. EMBO J. *35*, 1115–1132.

Maeshima, K., Tamura, S., and Shimamoto, Y. (2018). Chromatin as a nuclear spring. Biophys. Physicobiol. *15*, 189–195.

Maeshima, K., Tamura, S., Hansen, J.C., and Itoh, Y. (2020). Fluid-like chromatin: Toward understanding the real chromatin organization present in the cell. Curr. Opin. Cell Biol. *64*, 77–89.

Marshall, W.F., Straight, A., Marko, J.F., Swedlow, J., Dernburg, A., Belmont, A., Murray, A.W., Agard, D.A., and Sedat, J.W. (1997). Interphase chromosomes undergo constrained diffusional motion in living cells. Curr. Biol. *7*, 930–939.

Müller, S., Neusser, M., Köhler, D., and Cremer, M. (2007). Preparation of Complex DNA Probe Sets for 3D FISH with up to Six Different Fluorochromes. CSH Protoc. *2007*, pdb.prot4730.

Nakashima, K.K., Vibhute, M.A., and Spruijt, E. (2019). Biomolecular Chemistry in Liquid Phase Separated Compartments. Front. Mol. Biosci. *6*, 21.

Narlikar, G.J. (2020). Phase-separation in chromatin organization. J. Biosci. *45*, 5.

Nozaki, T., Imai, R., Tanbo, M., Nagashima, R., Tamura, S., Tani, T., Joti, Y., Tomita, M., Hibino, K., Kanemaki, M.T., et al. (2017). Dynamic Organization of Chromatin Domains Revealed by Super-Resolution Live-Cell Imaging. Mol. Cell *67*, 282–293.e7.

Olins, A.L., Gould, T.J., Boyd, L., Sarg, B., and Olins, D.E. (2020). Hyperosmotic stress: *in situ* chromatin phase separation. Nucleus *11*, 1–18.

Otterstrom, J., Castells-Garcia, A., Vicario, C., Gomez-Garcia, P.A., Cosma, M.P., and Lakadamyali, M. (2019). Super-resolution microscopy reveals how histone tail acetylation affects DNA compaction within nucleosomes in vivo. Nucleic Acids Res. *47*, 8470–8484.

Ou, H.D., Phan, S., Deerinck, T.J., Thor, A., Ellisman, M.H., and O'Shea, C.C. (2017). ChromEMT: Visualizing 3D chromatin structure and compaction in interphase and mitotic cells. Science *357*, eaag0025.

Perry, M., and Chalkley, R. (1982). Histone acetylation increases the solubility of chromatin and occurs sequentially over most of the chromatin. A novel model for the biological role of histone acetylation. J. Biol. Chem. *257*, 7336–7347.

Plys, A.J., Davis, C.P., Kim, J., Rizki, G., Keenen, M.M., Marr, S.K., and Kingston, R.E. (2019). Phase separation of Polycomb-repressive complex 1 is governed by a charged disordered region of CBX2. Genes Dev. *33*, 799–813.

Ricci, M.A., Manzo, C., García-Parajo, M.F., Lakadamyali, M., and Cosma, M.P. (2015). Chromatin fibers are formed by heterogeneous groups of nucleosomes in vivo. Cell *160*, 1145–1158.

Rogge, R.A., Kalashnikova, A.A., Muthurajan, U.M., Porter-Goff, M.E., Luger, K., and Hansen, J.C. (2013). Assembly of nucleosomal arrays from recombinant core histones and nucleosome positioning DNA. J. Vis. Exp. (79), 50354.

Sabari, B.R., Dall'Agnese, A., Boija, A., Klein, I.A., Coffey, E.L., Shrinivas, K., Abraham, B.J., Hannett, N.M., Zamudio, A.V., Manteiga, J.C., et al. (2018). Coactivator condensation at super-enhancers links phase separation and gene control. Science *361*, eaar3958.

Sanulli, S., Trnka, M.J., Dharmarajan, V., Tibble, R.W., Pascal, B.D., Burlingame, A.L., Griffin, P.R., Gross, J.D., and Narlikar, G.J. (2019). HP1 reshapes nucleosome core to promote phase separation of heterochromatin. Nature *575*, 390–394.

Schermelleh, L., Solovei, I., Zink, D., and Cremer, T. (2001). Two-color fluorescence labeling of early and mid-to-late replicating chromatin in living cells. Chromosome Res. *9*, 77–80.

Schwarz, P.M., Felthauser, A., Fletcher, T.M., and Hansen, J.C. (1996). Reversible oligonucleosome self-association: dependence on divalent cations and core histone tail domains. Biochemistry *35*, 4009–4015.

Shimamoto, Y., Tamura, S., Masumoto, H., and Maeshima, K. (2017). Nucleosome-nucleosome interactions via histone tails and linker DNA regulate nuclear rigidity. Mol. Biol. Cell *28*, 1580–1589.

Shimko, J.C., Howard, C.J., Poirier, M.G., and Ottesen, J.J. (2013). Preparing semisynthetic and fully synthetic histones h3 and h4 to modify the nucleosome core. Methods Mol. Biol. *981*, 177–192.

Stephens, A.D., Banigan, E.J., Adam, S.A., Goldman, R.D., and Marko, J.F. (2017). Chromatin and lamin A determine two different mechanical response regimes of the cell nucleus. Mol. Biol. Cell *28*, 1984–1996.

Stephens, A.D., Liu, P.Z., Kandula, V., Chen, H., Almassalha, L.M., Herman, C., Backman, V., O'Halloran, T., Adam, S.A., Goldman, R.D., et al. (2019). Physicochemical mechanotransduction alters nuclear shape and mechanics via heterochromatin formation. Mol. Biol. Cell *30*, 2320–2330.

Strick, R., Strissel, P.L., Gavrilov, K., and Levi-Setti, R. (2001). Cation-chromatin binding as shown by ion microscopy is essential for the structural integrity of chromosomes. J. Cell Biol. *155*, 899–910.

Strickfaden, H., McDonald, D., Kruhlak, M.J., Haince, J.F., Th'ng, J.P., Rouleau, M., Ishibashi, T., Corry, G.N., Ausio, J., Underhill, D.A., et al. (2016). Poly(ADP-ribosyl)ation-dependent Transient Chromatin Decondensation and Histone Displacement following Laser Microirradiation. J. Biol. Chem. *291*, 1789–1802.

Strickfaden, H., Missiaen, K., Hendzel, M.J., and Underhill, D.A. (2019). KMT5C displays robust retention and liquid-like behavior in phase separated heterochromatin. bioRxiv. https://doi.org/10.1101/776625.

Strom, A.R., Emelyanov, A.V., Mir, M., Fyodorov, D.V., Darzacq, X., and Karpen, G.H. (2017). Phase separation drives heterochromatin domain formation. Nature *547*, 241–245.

Tatavosian, R., Kent, S., Brown, K., Yao, T., Duc, H.N., Huynh, T.N., Zhen, C.Y., Ma, B., Wang, H., and Ren, X. (2019). Nuclear condensates of the Polycomb protein chromobox 2 (CBX2) assemble through phase separation. J. Biol. Chem. *294*, 1451–1463.

Thévenaz, P., Ruttimann, U.E., and Unser, M. (1998). A pyramid approach to subpixel registration based on intensity. IEEE Trans. Image Process. *7*, 27–41.

Thoma, F., Koller, T., and Klug, A. (1979). Involvement of histone H1 in the organization of the nucleosome and of the salt-dependent superstructures of chromatin. J. Cell Biol. *83*, 403–427.

Wang, L., Gao, Y., Zheng, X., Liu, C., Dong, S., Li, R., Zhang, G., Wei, Y., Qu, H., Li, Y., et al. (2019). Histone Modifications Regulate Chromatin Compartmentalization by Contributing to a Phase Separation Mechanism. Mol. Cell *76*, 646–659.e6.

Wang, L., Hu, M., Zuo, M.-Q., Zhao, J., Wu, D., Huang, L., Wen, Y., Li, Y., Chen, P., Bao, X., et al. (2020). Rett syndrome-causing mutations compromise MeCP2-mediated liquid-liquid phase separation of chromatin. Cell Res. *30*, 393–407.

Xiang, W., Roberti, M.J., Hériché, J.K., Huet, S., Alexander, S., and Ellenberg, J. (2018). Correlative live and super-resolution imaging reveals the dynamic structure of replication domains. J. Cell Biol. *217*, 1973–1984.

STAR★METHODS

KEY RESOURCES TABLE

REAGENT or RESOURCE	SOURCE	IDENTIFIER
Antibodies		
Mouse anti γH2A X	Millipore	05-636-1; RRID:AB_309864
Goat anti Mouse Alexa 488	Molecular Probes	A11001; RRID:AB_2534069
Chemicals, Peptides, and Recombinant Proteins		
α-Minimal Essential Medium	GIBCO	Cat. No. 12000-063
β-mercaptoethanol	Acros Organics	CAS Number 60-24-2
Alexa 488 C5 Maleimide	ThermoFisher	Cat. Number A10254
Alexa 647 C2 Maleimide	ThermoFisher	Cat. Number A20347
Aminoallyl-dUTP	Sigma Aldrich	CAS Number 936327-10-5
Aminoallyl-dUTP-Cy3	Jena Bioscience	NU-803-CY3-S
Aminoallyl-dUTP-XX-ATTO-488	Jena Bioscience	NU-803-XX-488-S
Ampicillin Sodium	GOLDBIO	CAS Number 69-52-3
Bovine Serum Albumin	Sigma Aldrich	CAS Number 9048-46-8
DH5α Cells	Hansen Lab	N/A
DraI	New England Biolabs	Cat. No./ID: R0129L
DTT	GOLDBIO	CAS Number 27565-41-9
EDTA	Fisher	CAS Number 60-00-4
EGTA	Sigma Aldrich	CAS Number 67-42-5
Ethanol	Sigma Aldrich	CAS Number: 64-17-5
Glacial Acetic Acid	Fisher	CAS Number 64-19-7
Glutaraldehyde	Sigma Aldrich	CAS Number 111-30-8
Glycerol	Fisher	CAS Number 56-81-5
Glycine	Sigma Aldrich	CAS Number 56-40-6
Guadinium HCl	Sigma Aldrich	G3272 - 500G
HaeII	New England Biolabs	Cat. No./ID: R0107L
HindIII-HF	New England Biolabs	Cat. No./ID: R3104L
Hoechst 33342	Sigma Aldrich	CAS Number 875756-97-1
Hydrochloric Acid	Millipore Sigma	CAS Number 7647-01-0
JQ1	Sigma Aldrich	CAS Number: 1268524-71-5
KCl	Sigma Aldrich	CAS Number 7447-40-7
KOAc	Fisher	CAS Number 127-08-2
LR White	Sigma Aldrich	CAS Number: 94188-59-7
LR White accelerator	Emsdiasum	14385
MatTek Dishes	MatTek	P35G-1.5-14-C
MgCl2 Hexahydrate	Fisher	CAS Number 7791-18-6
NaCl	Fisher	CAS Number 7647-14-5
NaOH	Fisher	CAS Number 1310-73-2
Paraformaldehyde	Sigma Aldrich	CAS Number 30525-89-4
PEG 6000	Millipore Sigma	CAS Number 25322-68-3
Phenol Chloroform Isoamyl alcohol 25:24:1	Ambion	Cat. No/ID: AM9732
Recombinant *Xenopus* Histone H2A	CSU Protein Purification Facility	N/A
Recombinant *Xenopus* Histone H2B	CSU Protein Purification Facility	N/A
Recombinant *Xenopus* Histone H3	CSU Protein Purification Facility	N/A
Recombinant *Xenopus* Histone H3 C110A	CSU Protein Purification Facility	N/A

(*Continued on next page*)

Continued

REAGENT or RESOURCE	SOURCE	IDENTIFIER
Recombinant *Xenopus* Histone H4	CSU Protein Purification Facility	N/A
Recombinant *Xenopus* Histone H4 E63C	CSU Protein Purification Facility	N/A
Saponin	Sigma Aldrich	CAS Number 8047-15-2
SDS	Fisher	CAS Number 151-21-3
Sodium bicarbonate	Sigma Aldrich	CAS Number 144-55-8
TAMRA succinimidyl ester	Sigma Aldrich	CAS Number 150810-68-7
TCEP HCl	GoldBio	CAS Number 51805-45-9
Trichostatin-A	Sigma Aldrich	CAS Number: 58880-19-6
TRIS-HCL	Sigma Aldrich	CAS Number 1185-53-1
Trizma base	Sigma Aldrich	CAS Number 77-86-1
XbaI	New England Biolabs	Cat. No./ID: R0145L
Yeast Extract	CRITERION	Cat. Number C7343
Critical Commercial Assays		
Effectene	Quiagen	Cat No./ID: 301425
Deposited Data		
Original/source data	This paper	https://data.mendeley.com/datasets/ty2xdkmt42/1
Experimental Models: Cell Lines		
C3H/10T1/2	ATTC	ATCC®CCL-226
Recombinant DNA		
601-207x12	Dr. S. Grigoryev	N/A
CBX5-Emerald	Dr. D. Alan Underhill	N/A
FOP-GFP (FGFR oncogenic partner)	Dr. E. Nigg	N/A
KMT5C-Emerald	Dr. D. Alan Underhill	N/A
PCNA-GFP 653	Dr. H. Leonhardt	N/A
Software and Algorithms		
Blender 2.8	Blender Foundation	RRID:SCR_008606
Fiji	https://fiji.sc	RRID: SCR_002285
Gatan Microscopy Suite	Gatan	RRID:SCR_014492
Illustrator CS 5.5	Adobe	RRID:SCR_010279
Imaris 9.5	Oxford Instruments	RRID: SCR_007370
Leica Application Suite X	Leica	RRID:SCR_013673
Microsoft Excel	Microsoft	RRID:SCR_016137
Photoshop CS 5.5	Adobe	RRID:SCR_014199
Prism 5	Graphpad	RRID:SCR_002798
Slidebook6	3i (Denver, CO)	RRID:SCR_014300
StackReg	P. Thevanez	http://bigwww.epfl.ch/thevenaz/stackreg/
UltraScan III Version 4.0	Borries Demeler	http://ultrascan.aucsolutions.com/index.php
Volocity 6.3	Quorum Technologies	RRID:SCR_002668
ZEN Digital Imaging For Light Microscopy	Zeiss	RRID:SCR_013672
Other		
Cascade II	Photometrics	https://www.photometrics.com
Colibri	Zeiss	Zeiss.com
CO2 Module S	Zeiss	411857-9010-000
GIF Tridiem 863 Energy filter	Gatan	https://www.gatan.com
Glass Bottom Dishes 14mM	MatTek Corporation	Part #: P35G-1.5-14-C

(*Continued on next page*)

Continued

REAGENT or RESOURCE	SOURCE	IDENTIFIER
HC FLUOTAR L 25x/0.95 W VISIR	Leica	Leica.com
Hypodermic 26.5 gauge injection needle	Becton Dickinson	305111
JEOL 2100F	JEOL	https://www.jeolusa.com/
Leica SP8	Leica	Leica.com
Objective 100X 1.4 Oil Plan APO	Zeiss	420790-9901-000
Objective "Plan-Apochromat" 40x/1.3 Oil DIC M27	Zeiss	420762-9800-000
Objective EC "Plan-Neofluar" 40x/1.3 Oil DIC M27	Zeiss	420462-9900-000
Objective 100x/1.40	Olympus	https://www.olympus-lifescience.com/en/objectives/detail/0-DIRECTORY%3A%3ADirFrontend-itemId.511706527.html
Olympus IX81	Olympus	https://www.olympus-lifescience.com/en/microscopes/inverted/ixplore-spin/
O2 Module S	Zeiss	411857-9040-000
Pecon CTi Controller 3700 digital	Pecon	Pecon.biz
PRISM BSI	Photometrics	https://www.photometrics.com/products/prime-family/primebsi
Sephacryl S1000 Beads	GE Healthcare	Cat. No/ID: 17-0476-01
Slim Bar Grids 300 Mesh	SPI	1161123
Temp Module S	Zeiss	411860-9010-000
UltraView	Perkin Elmer	https://www.perkinelmer.com/
Zeiss Axiovert 200M	Zeiss	https://www.zeiss.de/corporate/home.html

RESOURCE AVAILABILITY

Lead Contact

Further information and requests for resources and reagents should be directed to and will be fulfilled by Dr. Michael Hendzel (mhendzel@ualberta.ca).

Materials Availability

This study did not generate new unique reagents

Data and Code Availability

Original/source data for "Condensed chromatin behaves like a solid on the mesoscale in vitro and in living cells" have been deposited to Mendeley Data: https://dx.doi.org/10.17632/ty2xdkmt42.1.

EXPERIMENTAL MODEL AND SUBJECT DETAILS

For this study, we have used the female mouse embryonic fibroblast cell line C3H/10T1/2 (ATCC CCL-226). Cells were grown in α-MEM medium/10% Foetal Bovine Sera and propagated in 10 cm tissue culture plates at 37°C in a humidified incubator with 5% CO_2.

METHOD DETAILS

Fluorescently labeled dUTPs

Aminoallyl-dUTP-XX-Atto488, Aminoallyl-dUTP-XX-Atto594 and Aminoallyl-dUTP-Cy3 (each 1 mM) were purchased from Jena Bioscience (Germany). TAMRA-dUTP (~1 mM) was made by incubating TAMRA-succinimidyl ester with aminoallyl-dUTP in a bicarbonate buffer. 10 µl of 20 mM 10 µl aminoallyl-dUTP, 10 µl H_2O, 10 µl of 0.2M bicarbonate buffer and 20 µl of 10 mM of TAMRA-succinimidyl ester (total reaction volume 50 µl) were mixed in an Eppendorf tube and incubated for 3-4 hours at 30°C. To stop the reaction 2 µl of 2 M glycine (pH 8.0) were used. 4 µl of 1 M Tris-HCL (pH 7.8) were added to stabilize the nucleotides. In order to generate a concentration of 1 mM 200 µl H_2O were added (described in detail in Müller et al., 2007).

Preparation of chromatin fragments from cell nuclei and differential centrifugation assay for chromatin condensate formation

Cell nuclei were isolated by lysing cells from a 10 cm dish, containing approximately 6 million cells in lysis buffer (10 mM Tris-Cl, pH 7.5, 10 mM NaCl, 3 mM $MgCl_2$, 10 mM sodium butyrate, 250 mM sucrose and 0.25% V/V of NP-40). Nuclei were washed two times with same lysis buffer and were collected by centrifugation at 5000 rpm for 10 minutes. Nuclei were resuspended at 50 A260 units per ml in MNase digestion buffer (15 mM Tris–Cl pH 7.5, 15 mM NaCl, 250 mM sucrose, 2 mM $CaCl_2$, 60 mM KCl, 15 mM β-mercaptoethanol, 0.5 mM spermidine, 0.15 mM spermine, 0.2 mM PMSF, protease and phosphatase inhibitors) and were digested with 25 U/ml of micrococcal nuclease at 37°C for 20 min. The reaction was stopped by the addition of EGTA to 10 mM and nuclei were collected by centrifugation at 5000 rpm for 10 min. Nuclei were next resuspended in 10 mM EDTA for 30 min on ice, which resulted in nuclear lysis and the release of chromatin fragments into the medium. The EDTA soluble chromatin was separated from insoluble nuclear material by centrifugation at 10000 rpm for 15 min. The isolated soluble chromatin was dialyzed overnight against 1 mM Tris-Cl (pH 8.0) and 0.1 mM EDTA at 4°C. Soluble chromatin was collected after dialysis and this was incubated in defined concentrations of $MgCl_2$ at 4°C. Chromatin condensate formation was determined incubating chromatin in buffer (1 mM Tris-Cl (pH 8.0), 0.1 mM EDTA) containing $MgCl_2$ overnight at 4°C followed by centrifugation at 12500 rpm for 15 min. The absorbance of the supernatant at 260 nm was used as a measure of the chromatin that remained dispersed in solution (i.e., was not incorporated into chromatin condensates and pelleted by centrifugation).

Saponin labeling

Cells were grown to 60%–70% confluency prior to labeling. In order to bulk label cells with fluorescently labeled dUTPs for chromatin fractionation (see above), cells were treated with a wash buffer consisting of 20mM HEPES pH 7.5, 138mM, KCl, 4mM $MgCl_2$ and 3mM EGTA. After removing the wash buffer, a permeabilization buffer (wash buffer plus 0.04 μg/ml saponin) was added to the cells for 60 s. After carefully removing the permeabilization buffer, the wash buffer containing fluorescently labeled dUTP (50:1) was added carefully to the cells for 10 min. Subsequently the cells were incubated overnight in fresh DMEM.

Scratch labeling

Cells were labeled once they were approximately 80 percent confluent. The medium was completely removed from the cells and α-MEM containing fluorescently labeled dUTPs (50:1 dilution) was added so that all cells on the glass bottom were covered. The cell lawn was scratched with a 26-gauge hypodermic injection needle in parallel lines from one side to the other side. The dish was rotated 90° and the cell were scratched a second time as described above. After 2 minutes the cells were washed with 1 x PBS and incubated in fresh α-MEM until further usage (Schermelleh et al., 2001).

Inhibitor treatment

For the hyperacetylation experiments, the cells were incubated for 24h in 100 nM TSA before they were used in live-cell experiments once they reached 60%–70% confluency. To inhibit the BRD-acetylated lysine interactions, JQ1 inhibitors was added at a concentration of 2 mM to the cells 24 h before they were used in live-cell experiments.

Transfection

C3H/10T1/2 cells were transfected with expression plasmids at 60%–70% confluency the night before the experiments according to the protocol of the manufacturer: 100 μL Transfection buffer, 3 μL Enhancer 5 min incubation, 4 μL DNA (400ng/μl) 5 min incubation, 6 μL Effectene 20 min incubation.

Assembly and Purification of unlabeled recombinant histone octamers

Recombinant *Xenopus* core histones were purchased from the CSU Protein Expression and Purification facility. Reconstitution of unlabeled histone octamers was performed by first suspending lyophilized histones H2A, H2B, H3, and H4 in unfolding buffer (6M guanidinium HCl, 20mM Tris pH 7.5, 5mM DTT) for 2 h. Histones were mixed at equal molar concentration and then brought to a final protein concentration of 1mg/ml. The histone mixture was then dialyzed three times against 2 l of refolding buffer (2M NaCl, Tris pH 7.5, 1mM EDTA, 5mM β-mercaptoethanol) for 4h each to assemble histone octamers. The folded histone octamers were then concentrated using an Amicon Ultra-15 centrifugal filter and purified by size exclusion chromatography using the ATKA start liquid chromatography system and a HiLoad 16/60 Superdex 200 column. Peak fractions were run on an SDS polyacrylamide gel, and those fractions with equimolar amounts of the core histones were combined and concentrated to > 5mg/mL using a clean Amicon Ultra 15 centrifugal filter.

Alexa 488 H4 E63C labeling and labeled histone octamer assembly

Recombinant H4E63C was obtained from the CSU Protein Expression and Purification facility. Fluorophore labeling of histone H4 E63C was performed by adding an equimolar concentration of Alexa 488 C5 maleimide (Invitrogen) to histone in unfolding buffer in the presence of 0.7mM TCEP instead of DTT. Histone was then placed on a rotator and incubated in the dark overnight at 4°C. The fluorescently tagged H4 was then combined with suspended histones H2A, H2B, and H3 C110A in unfolding buffer, dialyzed against 2M NaCl refolding buffer, and the labeled octamers purified using size exclusion chromatography as described above.

Histone H3 C110A was used to prevent potential labeling of H3 with the Alexa 488 fluorophore during the procedure (Gibson et al., 2019a). Histones H4 E63C in combination with H3 C110A are commonly used for labeling of the histone octamer. H3 C110A does not affect nucleosome structure or positioning (Shimko et al., 2013).

Purification of 601-207bp x 12 template DNA

T Plasmid DNA containing the 601-207bp x 12 template from *E. coli* was purified by alkaline lysis. Purified plasmid was digested with enzymes XbaI and HindIII to release the template sequence, while enzymes HaeII and DraI where used to digest the vector DNA into smaller sizes. The larger ~2500bp template sequence was then separated from the digested vector fragments by gravity controlled size exclusion chromatography on a 115cm Sephacryl S-1000 column. Fractions containing only the template sequence were combined and ethanol precipitated. Template DNA was suspended in Tris pH 8.0, 10mM EDTA buffer to a final concentration of 1mg/mL prior to reconstitution.

Assembly of Alexa 488 labeled nucleosomal arrays

Nucleosomal arrays were reconstituted from the 601-207 bp x 12 DNA and purified histone octamers using a salt dialysis protocol. Unlabeled and fluorescently labeled histone octamers were combined at a ratio of 1:20 labeled to unlabeled octamer prior to reconstitution. Purified template DNA and histone octamers were mixed in TE buffer (10mM Tris pH 7.8, 1mM EDTA) containing 2M NaCl at a final DNA concentration of 0.3 mg/ml. The mixture was then dialyzed successively for 4 h against TE buffer containing 1.0M, 0.75M and 2.5 mM NaCl. The final dialysis step was against 10mM Tris pH 7.8, 0.25mM EDTA, 2.5mM NaCl, 0.1mM PMSF (TEN) buffer for 4 h. Only nucleosomal arrays that sedimented at 27-29S and contained 11-12 histone octamers/DNA template were used in subsequent experiments. Sedimentation coefficients were obtained using a Beckman XL-I analytical ultracentrifuge. Sedimentation velocity data were edited and analyzed with the UltraScan III program.

Chromatin condensate formation

Chromatin condensates were formed by first preparing buffer solutions containing either Tris-Cl pH 7.8 or Tris-(OAc) pH 7.5, the designated salts, and in some cases 5% [w/v] glycerol, 0.1 μg/mL BSA, or 5 mM DTT. Nucleosomal arrays were then added to the buffer solution to a final volume of 2mL and nucleosome concentration of 10 nM, rapidly mixed, and incubated for 20 min at 23°C.

Fluorescence microscopy and FRAP

Condensate volumes of 2mL were added to MatTek glass-bottom 35 mm Petri dishes with a 14 mm Microwell No. 1.5 cover glass slip and spun at 1,000xg for 3 minutes. Chromatin condensates were imaged and subject to photobleaching using an Olympus IX81 spinning disk confocal microscope, a 100x/1.40 numerical aperture objective, and a Photometrics Cascade II camera. Time-lapse images were collected every 10 s. Imaging software Slidebook6 (3I, Denver, CO) was used for image capture and analysis of fluorescence intensity and recovery after photobleaching. Representative images in Figures 1, S1, and S2 were obtained from the time-lapse series.

Assembly of Alexa 488 Labeled Nucleosomal Arrays

Nucleosomal arrays were generated using the 601-207 bp x 12 DNA template as previously described (Rogge et al., 2013). Histone octamers were combined at a ratio of 1:20 labeled to unlabeled octamer. All arrays were validated to be at or near saturation (27-28 S) using analytical ultracentrifugation as previously described (Rogge et al., 2013). Arrays were stored in a final buffer of 10mM Tris pH 7.8, 2.5 mM NaCl, 0.25 mM EDTA after dialysis.

Chromatin condensate formation and Fluorescence Microscopy/photobleaching

Chromatin condensates were formed by first preparing the buffer solutions containing either Tris-Cl pH 7.8 or Tris-(OAc) pH 7.5 and the designated salts, 5% [w/v] glycerol, 0.1 μg/mL BSA, or 5 mM DTT. Arrays were then added to the solution to a final nucleosome concentration of 10 nM, rapidly mixed, and incubated for 20 min at 23°C. The samples where then added to MatTek glass bottom 35 mm Petri dishes with a 14 mm Microwell No. 1.5 cover glass and spun at 1,000 g for 3 minutes. Chromatin condensates were imaged and subject to photobleaching using an Olympus IX81 spinning disk confocal microscope, a 100x/1.40 numerical aperture objective, and a Photometrics Cascade II camera. Time lapse images were collected every 10 s. Imaging software Slidebook6 (3I, Denver, CO) was used for image capture and analysis. Representative images in Figure 1 were obtained from zoomed in crops of the unfiltered time lapse videos.

Fixation of cells

For fixation, cells were washed once with 1x PBS pH 7.2 and then fixed in 1 x PBS pH 7.2 with 4% paraformaldehyde for 10 minutes. For electron microscopy, cells were fixed in a 2% glutaraldehyde and 4% paraformaldehyde fixative in PBS pH 7.2. For fixing cells with hypercondensed chromatin cells were incubated in a 560 mOsm PBS solution and then fixed at 560 mOsm in a fixative containing 2% glutaraldehyde and 4% paraformaldehyde.

Fluorescence microscopy (Fractionated Chromatin/in-vivo)

20 min prior to observation, cells/chromatin was stained with 0.5 μg/ml of Hoechst 33342. Photobleaching, laser micro-irradiation and time-lapse experiments were carried out on a spinning disk microscope equipped with a 100x 1.4 NA oil immersion objective lens, 405, 488, and 561 nm solid state laser lines and a photokinesis device. During the experiments, cells were kept at 37°C in humidified atmosphere containing 5% CO_2. Cells were able to divide normally after photobleaching (Video S5). Replication-labeled chromatin was photobleached or laser microirradiated by drawing a region of interest (ROI) onto the nuclear areas in Volocity and then exposing the marked areas to intense laser-light of the chosen laser-lines to photobleach (488 nm or 561 nm) or microirradiate (405 nm) the chromatin. For photobleaching, the following parameters were used: Tamra-dUTP was photobleached using 66% power of the 561 nm solid state laser-line and 10 iterations. Cy3-dUTP was photobleached using 75% power of the 561 nm solid state laser-line and 10 iterations. Atto594-dUTP was photobleached using 75% of the 561 nm solid state laser line and 10 iterations. Atto488-dUTP was photobleached using 75% of the 488 nm solid state laser line and 10 iterations. To photobleach the Emerald-tagged fluorescent proteins (CBX5/KMT5C) 50% power of the 488 nm solid state laser-line and 10 iterations were used. For the laser micro-irradiation experiments, 20% power of the 405 nm solid state laser and 10 iterations were used to induce DNA damage.

Hyper- and Hypotonic treatment of cells

Hypertonic treatment was applied to cells by adding medium that was mixed with a 10x PBS solution in the ration 1:10 in order to reach a concentration of 560 mOsm. Hypotonic treatment was applied by adding deionized, distilled water to the medium (1:1). See Albiez et al. (2006) for details.

Electron Spectroscopic Imaging

ESI was performed using a JEOL 2100F transmission electron microscope with a LaB6 filament operating at 200 kV. A Tridiem GIF post column spectrometer (Gatan) was used to record the elemental maps of phosphorus and nitrogen. Phosphorus maps were created by recording post-edge images at 175 eV electron energy loss with a slit-width of 20 eV and a pre-edge image at 120 eV electron energy loss with a slit-width of 20 eV. Phosphorous maps were created by normalizing the background signal in void regions of the post-edge images to the background signal in pre-edge images and then subtracting the pictures. Nitrogen maps were processed by dividing post-edge images (recorded at 447 eV electron energy loss with a slit-width of 35 eV) by pre-edge images (recorded at 358 eV with a slit-width of 35 eV). Noise in the elemental maps was decreased by using a median filter with the radius 1 in FiJI/ImageJ.

Test for DNA damage by nucleotide incorporation

Cells were tested for potential DNA-damage caused by incorporation fluorescent nucleotides by fixing C3H/10T1/2 cells 12.5h and 24h after replication labeling and doing immunofluorescence labeling with a monoclonal primary antibody against γ-H2AX as a marker for DNA damage (Figure S5). As secondary antibody a goat-anti-mouse Alexa 488 antibody was chosen. Chromatin was stained with Hoechst (which served as a mask) and a large area was scanned using the "Navigator" module in LAS X on a Leica SP8 confocal microscope. Areas that included 387 nuclei (12.5h) and 537 (24h) respectively were recorded using a 25x water objective (see Figure S5). The integrated intensity of the Alexa 488 and TAMRA signal was determined for each nucleus in Imaris and the values were plotted using Prism.

QUANTIFICATION AND STATISTICAL ANALYSIS

Data acquired at the spinning disc confocal microscope were exported from Volocity as ome.tiff for further processing in FiJI or Imaris.

Motion compensation of whole nuclei was corrected using the plug-in "Stack-Reg" (Thévenaz et al., 1998).

Quantification of photobleaching was performed in FiJI by determining the mean intensities of regions of interest in the bleached areas before, immediately after and 30 min after photobleaching. The intensity values were normalized in Prism and the average intensities and standard deviations across all experiments were calculated. These were tested for significance in prism using the t test.

Imaris was used to track the replication foci in time after laser micro-irradiation to show the expansion of the chromatin after DNA-damage (Figure S4). Replication foci were manually identified, and "Spots" were placed at their intensity maximum in each frame of the observation. Spots representing one replication focus over time were joined into a "Track" and the xy coordinates of the spots of a track were exported into a CSV, which was further processed in Microsoft Excel (v16.39).

The gravity center of the measured points at a certain time point was determined according to the formula: $x_s = \frac{1}{M} \sum_{i=0}^{n} x_i \cdot m_i$. The average distance of individual replication domains to the center of gravity at a certain time point was calculated: $|x| = x_i - x_s$.

3D volume renderings of the replication labeled chromatin domains that were exposed to different osmotic environments the "Surface" tool were generated in Imaris using the "Surfaces" tool from the 3D microscopic data.

VRML2 (*.wrl) files exported from Imaris and imported into Blender were ray-traced using the cycles render engine.

Volumes of nuclei and chromocenters in changing osmotic environments (Figure S6) were determined by using the ''Surface'' tool in Imaris. The volumes of the nuclei/chromocenters were normalized by setting the initial volume to 100 and plotted in Prism.

Data processing

Volocity 6.3

Data acquired at the spinning disc confocal microscope were exported as ome.tiff for further processing in FIJI or Imaris.

FIJI

Motion compensation of whole nuclei was corrected using the plug-in ''Stack-Reg'' (Thévenaz et al., 1998). FRAP-Curves were generated using the ROI-Manager and its ''Multi-Measure'' function.

Imaris® 9.5

Imaris was used to create supporting online movies or 3D reconstructions from the recorded image stacks. The Volumes of the chromocenters and its replication labeled chromatin domains were carried out by using 3D stacks of and fitting volumes of these structures with the ''Surfaces'' tool. The respective surfaces were then exported in the VRML2 (.wrl) format for further processing in Blender.

Blender 2.8

VRML2 files containing surfaces of chromocenters generated by Imaris® 9.5 were imported in Blender and ray-traced using the cycles render engine.

Digital Micrograph®

TEM pictures were recorded using Digital Micrograph®

Ultrascan III®

Sedimentation coefficients were derived from sedimentation velocity data using the van Holde/Weischet analysis module

Slidebook 6

Slidebook was used for image capture and analysis of fluorescence intensity and recovery after photobleaching of the *in vitro* chromatin condensates

Photoshop

Figures were assembled using Adobe Photoshop®.

Image Processing for Figure Creation

16-bit images recorded at the spinning disc microscope were exported in Volocity to the OME-TIFF format and background subtracted in ImageJ by the average signal intensity in an empty area + the SD of the signal therein. Subsequently, the ImageJ function ''Histogram'' was used to determine the brightest pixel. The range of displayed intensities was adjusted in ''Brightness & Contrast'' by manually entering the intensity value of the brightest pixel as the upper limit and zero as the lowest limit. After converting the images to 8-bit and merging them in the RGB space, representative nuclei and regions of interest were assembled to figures in Photoshop. In order to avoid artifacts, the ''nearest neighbor'' algorithm was chosen to enlarge regions of interest.

Supplemental Figures

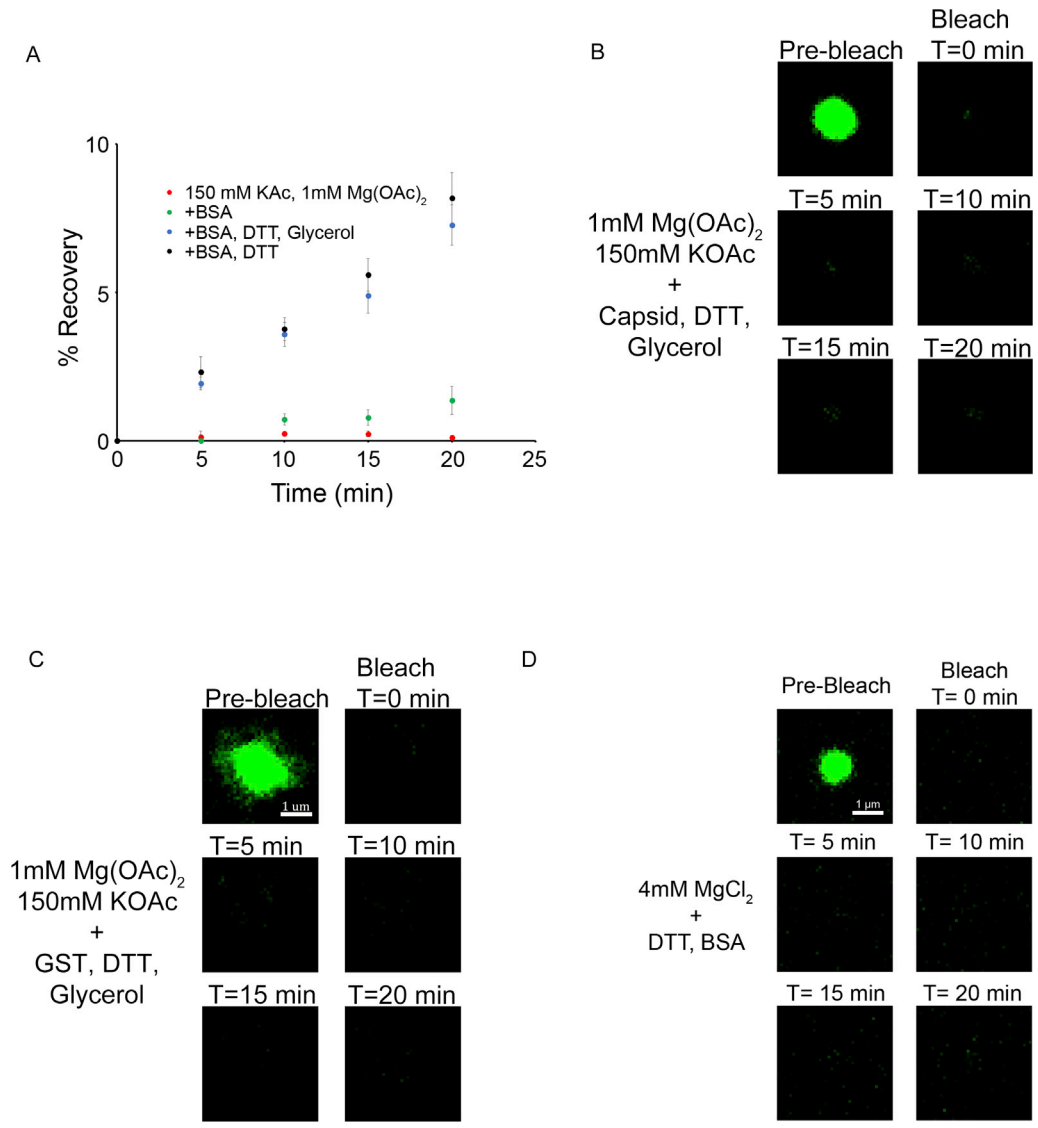

Figure S1. Photobleaching of Entire Chromatin Condensates and Condensate Liquidity Is Not Observed in the Presence of GST or Severe Acute Respiratory Syndrome Coronavirus 2 (SARS-CoV-2) Nucleocapsid Protein, Related to Figure 1

(A) Fluorescence recovery after photobleaching of entire chromatin condensates formed by Alexa488 labeled nucleosomal arrays in 4mM $MgCl_2$, BSA, and DTT (Scale bar, 1μm).

(B) Graphical representation of percent fluorescence recovery after photobleaching of condensates from Figures 1C–1F (n = 4 condensates per condition. Error Bars Represent Standard Error of the Mean).

(C) Fluorescence recovery after photobleaching of a chromatin condensate formed by Alexa488-labeled nucleosomal arrays in buffer containing 1.5μM GST protein, 1mM $Mg(OAc)_2$, 150mM KOAc, Glycerol and DTT (Scale bar, 1μm).

(D) Fluorescence recovery after photobleaching of chromatin condensate formed by Alexa488-labeled nucleosomal arrays in buffer containing 1.5μM SARS-CoV-2 Nucleocapsid phosphoprotein, 1mM $Mg(OAc)_2$, 150mM KOAc, Glycerol and DTT.

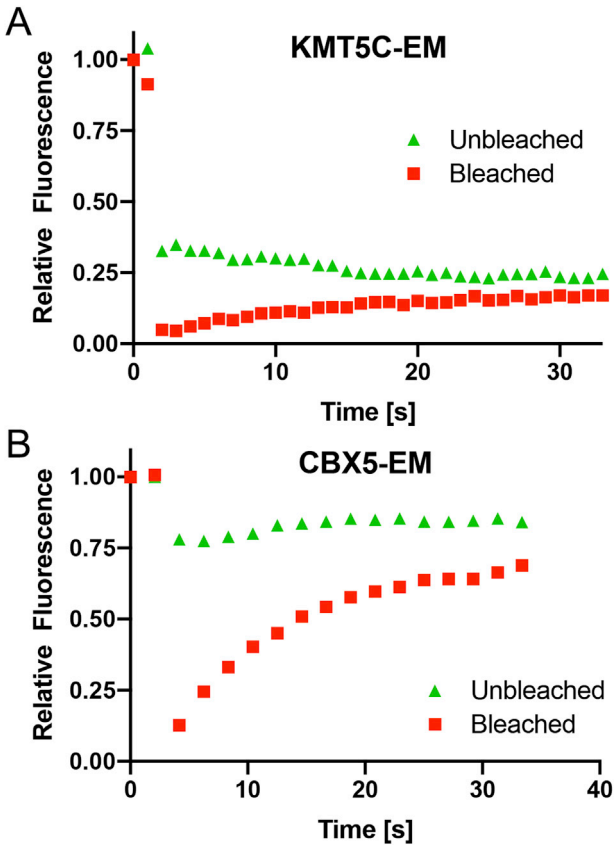

Figure S2. Photobleaching of KMT5C-EM and CBX5-EM after Photobleaching Parts of a Chromocenter, Related to Figure 2

(A) Photobleaching of a region of a chromocenter in KMT5C-Emerald-transfected cells reveals slow recovery of the protein in the bleached area (red line). The parallel loss of fluorescence in the non-bleached part of the chromocenter (green line) reveals that the recovery is primarily arising from redistribution of the KMT5C-Emerald within the chromocenter.

(B) Photobleaching of a region of a chromocenter in CBX5-Emerald-transfected cells reveals rapid recovery in the bleached area (red line) and only a modest loss of signal in the unbleached portion (green line) of chromocenter. This indicates that much of the CBX5-Emerald reflects substantial influx of fluorescent CBX5 from the nucleoplasm rather than redistribution of the chromocenter population observed for KMT5C.

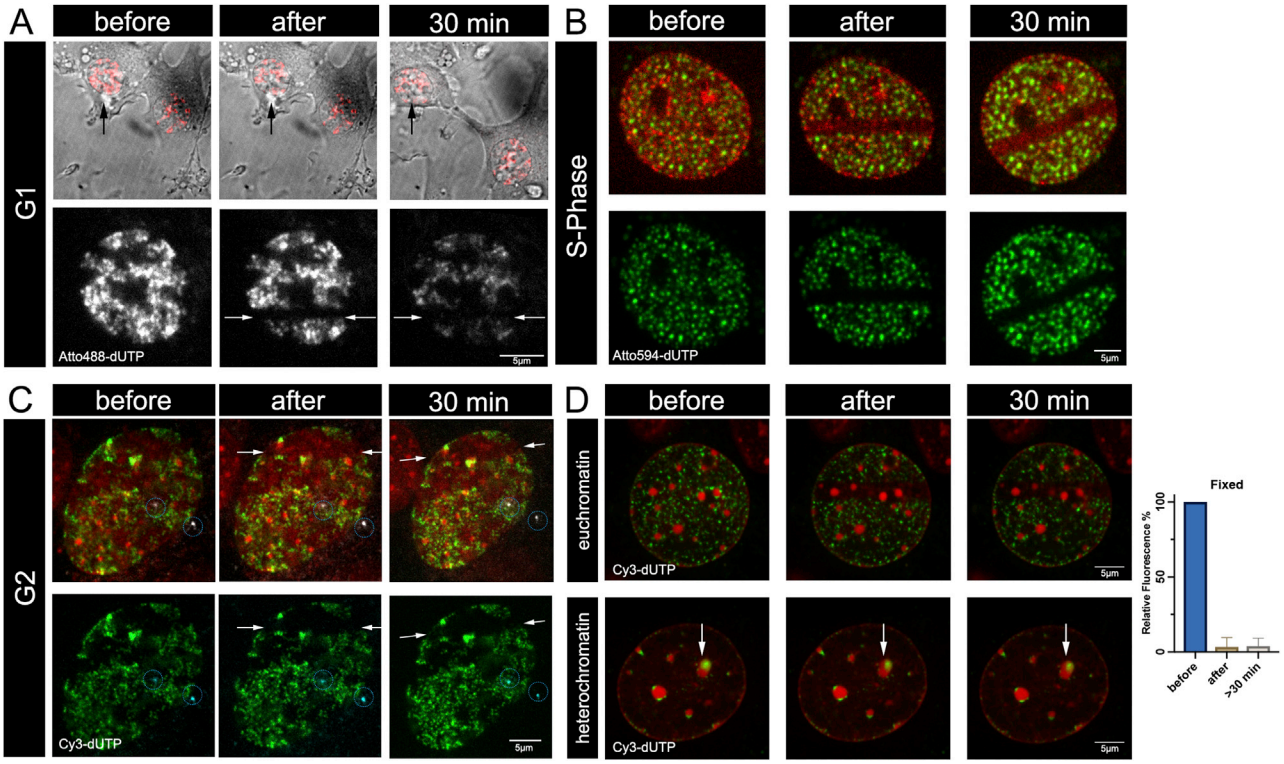

Figure S3. Photobleached Fluorescent Chromatin Does Not Recover in All Phases of Interphase and in Fixed Cells (Control), Related to Figure 2

(A) Lack of fluorescence recovery of fluorescent, replication-labeled chromatin in a G1 phase C3H/10T1/2 nucleus shortly after mitosis. Upper: Merged transmitted light and Cy3 channels reveal that the daughter cells are still in the process of completing cytokinesis. Lower: Fluorescent chromatin in the left daughter nucleus is photobleached and fails to show recovery of fluorescence after 30 min.

(B) C3H/10T1/2 nucleus showing an early S-Phase labeling (green), transiently transfected with PCNA-GFP (red) to identify S-Phase cells, does not show recovery of replication labeled chromatin after photobleaching in S-Phase. The top row shows replication-labeled chromatin (green) and PCNA (red). The bottom image series shows the replication-labeled chromatin alone.

(C) C3H/10T1/2 nucleus in late G2 (identified based on centrosome duplication and separation) does not show recovery of photobleached replication labeled chromatin after photobleaching. The top row shows a merged image of Hoechst (red), Cy3-dUTP (green) and the centrosome marker FGFR1 Oncogene Partner (FOP)-GFP (white and outlined by cyan circles). The bottom row shows Cy3-dUTP (shown in green) and FOP-GFP (shown in cyan outlined by cyan circles).

(D) Axial drift and detector noise can contribute to variation in signal when signal intensities are low. To test for the stability of the signal in the absence of biological activity, we fixed replication-labeled C3H/10T1/2 cells with paraformaldehyde and then performed photobleaching. The results show that low amounts of signal recovery can be observed in cells that cannot undergo actual recovery. Thus, instrumental sources of variation, in particular, small amounts of axial drift, result in small changes in fluorescence intensity in the absence of actual changes in the distribution of the fluorescent molecules. The chromocenter highlighted with a dashed yellow circle illustrates the small amount of axial drift and how it can impact the total signal obtained. The size and intensity of this chromocenter decline slightly reflecting a small change in the axial position over the 30-minute imaging period.

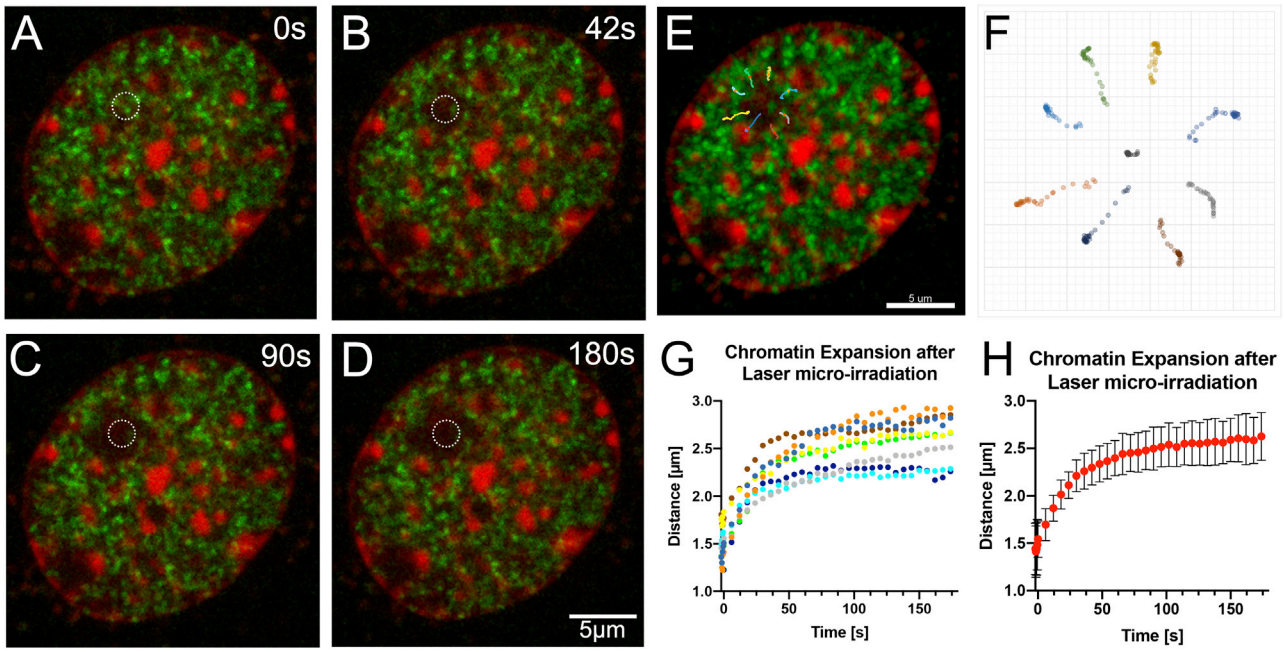

Figure S4. Rapid Dispersion of Chromatin in Response to Laser Microirradiation, Related to Figure 4

(A–D) Expansion of the chromatin shown at different time points.

(E) Nucleus showing eight tracked replication domains forming a starburst pattern as the more centrally-located damaged chromatin expands and displaces the surrounding chromatin.

(F) Tracks shown in E and the geometric gravity center of the points at every observed time point shows very similar expansion of the chromatin away from this center (isometric expansion).

(G) Distance from the center in time for all tracked replication domains shown in (E) and (F). The dynamics of the expansion are similar for the tracked replication domains.

(H) shows the mean distance traveled for the tracked points showing small variance between the points (error bars).

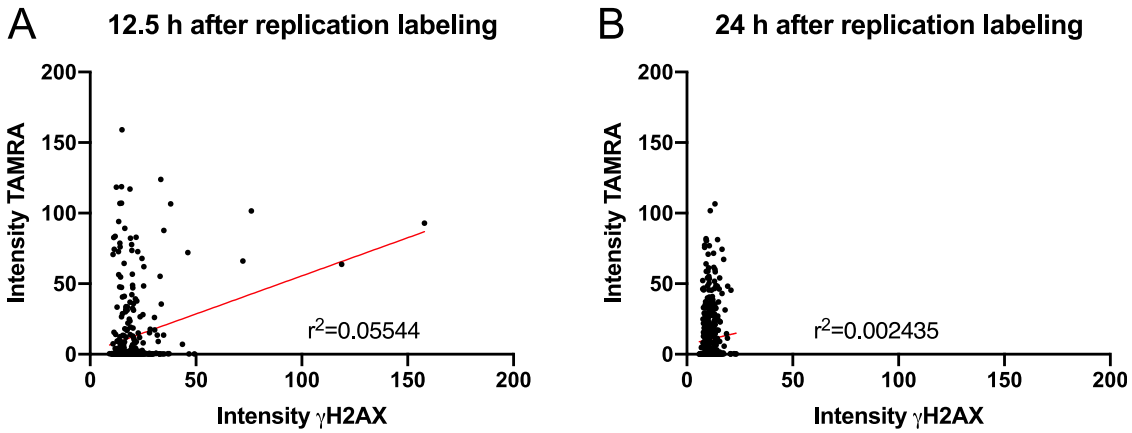

Figure S5. Reversible Osmolarity-Dependent Changes in Nuclear and Chromocenter Volume of Living Cells Related to Figure 5

The volumes of nuclei and chromocenters were measured in living cells exposed to different osmolarities. Iso represents the initial volume of cells in normal iso-osmolar medium (~290 mOsm, Iso1) before incubating the cells in hyper-osmolar medium (~560 mOsm, Hyper), returned to iso-osmolar medium (~290 mOsm, Iso2) and hypo-osmolar medium (~140 mOsm, hypo).

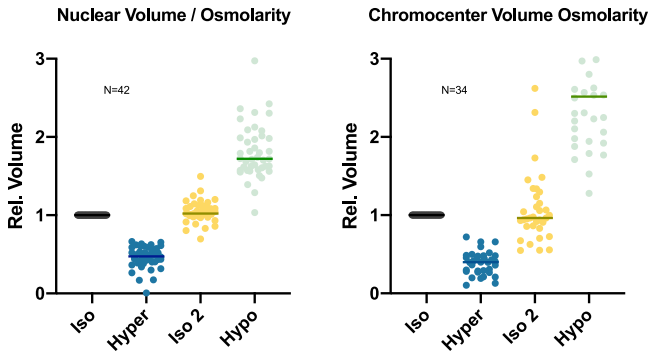

Figure S6. Testing for DNA Damage following Replication Labeling, Related to STAR Methods

The average intensities of a marker for DNA double-strand breaks, gH2AX, and dUTP-TAMRA within nuclei were plotted relative to each other and show very low correlations between DNA-damage and replication label intensity for cells labeled (A) 12h and (B) 24h prior to staining, respectively.